Journal of the Franklin Institute 361 (2024) 106934

Contents lists available at ScienceDirect

Journal of the Franklin Institute

journal homepage: www.elsevier.com/locate/fi

Optimal control strategies for PMSM with a decoupling super twisting SMC and inductance estimation in the presence of saturation

Tanja Zwerger [a], Paolo Mercorelli [b,*]

[a] Department of Development, Rolls Royce Solutions GmbH, Maybachplatz 1, Friedrichshafen, D-88045, Germany
[b] Institute for Production Technology and Systems, Leuphana University of Lueneburg, Universitaetsallee 1, Lueneburg, D-21335, Germany

ARTICLE INFO

Keywords:
ST-SMC
PMSM
EKF
MTPA
Kalman filter

ABSTRACT

This paper deals with optimal control strategies robustified by a decoupling super-twisting sliding mode control (ST-SMC) for permanent magnet synchronous machines (PMSM). In general, ST-SMC is a robust method for controlling systems and guarantees asymptotic convergence in cases where the upper bound of model uncertainties such as disturbances and parametric uncertainties is not known a priori, if the upper bound of the derivative is known. The proposed optimal control strategy is designed for a constant torque reference whose control is implemented in two control regions: maximum torque per ampere (MTPA) and flux-weakening control. In the proposed analysis, the operating point of the motor can also be in the saturation region, which makes the estimation of L_d and L_q in the proposed optimization procedure of particular interest and also important for the decoupling control implemented with ST-SMC. To compensate for typical parameter variations, adaptive parameter estimation is introduced into the control system using an extended Kalman filter (EKF) in combination with a bivariate polynomial. In order to be able to make an assessment of the control performance of the ST-SMC, a comparison with a conventional PI controller is shown at the end of the paper. Measured results using hardware in the loop (HIL) to validate the results and their detailed discussion and analysis are included.

1. Introduction and motivation

Permanent magnet synchronous machines (PMSMs) are highly recommended for all applications where high energy densities are required. In fact, PMSMs are highly efficient electric motors for a wide range of applications. As the name suggests, this motor technology requires magnetic material in the rotor. In the proposed analysis, the operating point of the motor can also run in saturation regions and thus the estimation of L_d and L_q is of particular interest in the proposed optimization procedure and also for the decoupling control realized with help of super-twisting sliding mode control (ST-SMC) to minimize the amplitude of its switching gains. The typical parameter fluctuations are compensated by estimation with an extended Kalman filter (EKF). By estimating the current-dependent parameters, the optimization method becomes robust. In fact, the optimization procedure based on Lagrange method is strongly depending on the variation of the parameters of the model. Secondly, the decoupling strategy that minimizes the PI variation in [1] depends on the variations of the parameters. Finally, the equivalent part of the sliding mode control (SMC) depends on the variation of the parameters, and if an adaptive estimation of these parameters is made, small switching gains are

* Corresponding author.
E-mail address: paolo.mercorelli@leuphana.de (P. Mercorelli).

https://doi.org/10.1016/j.jfranklin.2024.106934
Received 28 October 2023; Received in revised form 11 May 2024; Accepted 16 May 2024
Available online 23 May 2024

The main nomenclature

$u_d(t)$	direct voltage input
$u_q(t)$	quadrature voltage input
$i_d(t)$	direct current
$i_q(t)$	quadrature current
$i_{dd}(t)$	desired direct current
$i_{qd}(t)$	desired quadrature current
$\mathbf{I_d}$	measured current vector i_d
$\mathbf{I_q}$	measured current vector i_q
$\mathbf{L_{dD}}$	measured inductance vector L_d
$\mathbf{L_{qD}}$	measured inductance vector L_q
$\omega_{el}(t)$	electrical angular velocity of the rotor
p	pair of magnetic poles ($\omega_{el}(t) = p\omega_r(t)$)
R_s	coil resistance
$L_d(t)$	direct axis self-inductance
$L_q(t)$	quadrature axis self-inductance
$\hat{L}_{d/q}(t)$	estimated direct and quadrature axis self-inductance
$\hat{i}_{d/q}(t)$	estimated direct and quadrature axis currents
Ψ_p	main flux constant
$\psi_d(t)$	direct flux component
$\psi_q(t)$	quadrature flux component
$T(t)$	torque
$T_d(t)$	desired torque
$\mathbf{\Theta}_d$	coefficient polynomial for calculation of L_d
$\mathbf{\Theta}_q$	coefficient polynomial for calculation of L_q
$\theta_{el}(t)$	electrical angle of the rotor
Lag	Lagrangian function

guaranteed, as already explained. Application examples for the control of PMSMs using different types of SMC are also well analyzed in [2,3], where speed control with self-triggered SMC is presented. Self-triggering is used to reduce the communication frequency for controlling the networked PMSM. For current control within a variable speed range, the PMSM operates in different ranges. In the constant torque range, the limit of the maximum current must be maintained. At the same time, it is important to reduce the copper losses of the PMSM, which are essentially caused by the current impression.

1.1. Control strategies for PMSMs

Maintaining the desired torque while limiting the current to a minimum value presents an initial optimization problem: The so-called maximum torque per ampere (MTPA) is a well-known approach, as can be seen in [4], where a normalized MTPA calculation is performed for a PMSM with reluctance torque. Also taking into account the maximum allowed voltage, the maximum torque must be determined, which is the definition of another optimization problem. This can be solved by using the so called maximum torque per voltage (MTPV) optimization approach. Although MTPA and MTPV are consolidated optimization strategies, they are still the subject of research. Indeed, in [5], the authors recently proposed a new optimal online tracking method with improved MTPA and MTPV considering the magnetic core saturation effect. Typically, the control is a PI control with a feedforward action for decoupling the coupled branches in a PMSM. Once the electrical part of the system is decoupled (see, for example, [1]), various control techniques can be used. Another control approach is described by the usage of the SMC, which is described as a type of variable structure control and which has been implemented in the 1950s. The SMC is known as a robust control type for linear and nonlinear systems and describes a nonlinear design process. Due to its insensitivity against parameter uncertainties, it can have advantages regarding the control of an electrical machine, especially in a saturated condition as it can occur for higher torque demands. The classical SMC is a first order SMC, with a first degree sliding surface. The SMC uses for its control a discontinuous control signal, which ensures the control on a sliding surface. The main disadvantage of the SMC is the chattering at the output at the system, which can cause damage to, for example, inverters because of resulting current peaks. This resulting disadvantage led to the introduction of the ST-SMC, which is a type of second-order SMC and was introduced in 1993 by Levant in [6]. The advantage of higher-order ST-SMC is that a continuous control function is generated, which results in the moving variable and its derivative being brought to zero in finite time. More recently, in [7], two composite current controllers, each combining two ST-SMCs, are proposed for the drive system of a synchronous reluctance motor considering magnetic self-saturation and cross-saturation. Theorem

1 in [7] is the theoretical guideline for selecting the gain of the conventional ST-SMC, which requires the a priori knowledge of the upper limit of the derivative of the lumped disturbance. In this proposed contribution the same control law as in [8] and in [9] in which it is shown that ST-SMC is a robust method for controlling systems without a priori knowledge of the upper bound of model uncertainties such as disturbances and parameter deviations and guarantees asymptotic convergence. However, it is required that the derivative of the disturbance is bounded, but not the upper bound of the disturbance.

1.2. ST-SMC for PMSM

The efficiency, high power density and adaptability of PMSMs have brought them to the forefront for a variety of industrial applications in recent years. To realize the full potential of PMSMs, in-depth control systems are required to ensure precise and reliable operation [10]. ST-SMC, one of these techniques, stands out as a possible tool for improving PMSM performance under severe load conditions. The theory, practice, advantages and disadvantages of using ST-SMC for PMSMs are examined in this literature review [11]. The ST-SMC is a robust control method that traces the states of a system along a sliding manifold back to the origin to stabilize its dynamics. The ST-SMC is a variant of the SMC that uses higher order sliding modes, resulting in higher convergence speed and lower chattering. This method is an attractive option for PMSM control and is characterized by robustness with respect to the presence of model uncertainties, disturbances, and nonlinearities [12] or [13]. When it comes to dealing with the difficulties posed by parameter variations, external disturbances, and model uncertainties, the ST-SMC approach provides an impressive level of robustness [14]. The higher order sliding modes of the ST-SMC are responsible for the resilience of the algorithm, which enables fast convergence and precise tracking of the desired trajectories [15]. As a result, PMSM systems show significant performance gains in both transient and steady-state behavior when operated with ST-SMC [16] or [17,18]. A major advantage of ST-SMC is that it significantly reduces chatter compared to other SMC techniques. The super-twisting algorithm, which is vital for reducing chatter, is widely used by ST-SMC. This improvement in running smoothness means that the electrical machine is subjected to less mechanical stress and consequently less wear, which can extend its service life. Since nonlinear behavior is characteristic of PMSM systems with reluctance torque, ST-SMC elegantly accounts for this behavior without requiring a precise model of the system. ST-SMC is characterized by its nonlinear adaptability, which enables it to handle the complexity of PMSM dynamics and performance. Due to its robustness to model uncertainties, fast response times, chatter suppression and ability to navigate through intrinsic nonlinear characteristics, ST-SMC proves to be a comprehensive control approach for PMSM systems. PMSMs are of critical importance in electric vehicles (EVs) due to their high torque density and high efficiency. ST-SMC builds on the strengths of PMSMs in electric vehicles by improving the accuracy of torque control and thus the efficiency of the system. This improvement directly contributes to extending battery life and increasing the range of electric vehicles. ST-SMC plays a crucial role in realizing the full potential of PMSMs in the context of sustainable mobility by optimizing the use of power and resources [19]. Wind energy conversion systems (WECS) take advantage of PMSMs and harness the power of the wind to generate electricity [20]. It is becoming clear that the integration of ST-SMC into these systems is critical to achieve both maximum power generation and smooth grid integration. ST-SMC expertly controls volatile wind conditions and ensures that power generation remains stable and in phase with the grid even when there is no wind. The critical function of ST-SMC in improving the efficiency and reliability of wind power systems cannot be overstated. Applications using PMSM-equipped robotic arms highlight the need for precise motion control in the field of robotics. In this context, ST-SMC proves to be an organizing principle that helps these robotic systems to follow their trajectories precisely and to manipulate them smoothly. By using ST-SMC, robotic arms are able to perform even the most complex tasks with the highest accuracy, opening up new possibilities for robotic systems in manufacturing, healthcare, and academia [21]. The performance of PMSMs can be improved by using ST-SMC, which has proven to be a reliable and successful method. Its ability to deal with model uncertainties, disturbances, and nonlinearities makes it well suited for real systems. It is expected that further improvements in controller design, parameter tuning, and hardware implementation will increase the prevalence of ST-SMC in PMSM-based systems and enhance their efficiency, reliability, and overall performance as research in this area continues [22].

1.3. Estimation of inductance

The estimation of the inductance is extremely important in the context of the optimization procedures. It is known that any optimal control strategy is based on a model and therefore its solution depends on the parameters of the model that need to be estimated. In particular, the estimation of the inductance is important in the proposed problem, because saturation changes the value of the inductance. To get an impression of existing estimation methods for the parameter estimation of inductances in PMSMs, the review in [23] gives a very good overview. The main difference between the estimation methods listed there is that saturation is not included and only nominal values are considered for the estimation. However, the estimation method presented here is able to take saturation into account by introducing the bivariate polynomial into the EKF. The Kalman filter (KF) and especially the EKF is a feasible approach and shows effectiveness and easy to implement solutions for this type of problems. In [24], a motion sensorless control of an internal combustion engine using EKF is proposed. In [25–27], different control strategies are applied using virtual sensors based on EKF.

1.4. Contribution of the results and structure of the paper

The main contributions of the paper consists of a combination and harmonization of different control strategies supported by an optimal observer using KF:

- an optimal control strategy, designed for constant torque reference for PMSM and is made robust by a decoupling ST-SMC.
- An EKF is used to estimate the inductance of the PMSM to adapt the proposed ST-SMC, which is a robust method to control systems without a priori knowledge of the upper bound of model uncertainties and disturbances in case of asymptotical convergence.
- an optimal control strategy is investigated in two control ranges: MTPA for constant torque range and flux weakening control for constant power range.
- a compensation for typical parameter variations is done by an adaptive parameter estimation, which is introduced into the control system using an EKF in combination with a bivariate polynomial.
- measured results using hardware in the loop (HIL) are presented where the control performance of the ST-SMC is compared with a conventional proportional integral (PI) controller.

Considering the last point of the contributions, it is possible to conclude that the aim of using HIL as an emulator for validation is to establish the functionality of the presented estimation method both in the saturation region and under the influence of cross-coupling effects as well as spatial harmonics. The neglect of temperature effects as well as losses in the iron core is permissible in order to verify the functionality of the mentioned methods and it justifies the use of a HIL emulator for the experimental verification. The paper is organized as follows. Section 2 presents the physical and mathematical model of PMSMs. Section 3 discusses MTPA and a flux weakening approach. Then, a decoupling ST-SMC approach for a PMSM application is presented in Section 4, and an EKF for inductance estimation even in saturated regions is presented in Sections 5 and 6. The paper continues with Section 7, where HIL measurements and results show the validation of the proposed control scheme. Section 8 is dedicated to a detailed discussion and analysis of the results in relation to the role of the different elements of the proposed control strategy. A conclusion closes the paper.

2. The physical and mathematical model of PMSMs

The most common control of PMSM is the use of field-oriented control. For this, the three-phase model of the electrical machine, which works with sinusoidal variables, is converted into a constant variable model. The conversion takes place with the aid of the so-called Clarke–Parke transformation. By the conversion into a system of equal quantities, a control for the so-called d- and q-axis can be constructed. The cross coupling cannot be neglected. Rather, it describes both a premagnetization of the q-axis by the d-current and a premagnetization of the d-axis by the q-current. The decoupling is achieved by feedforward control and is an essential measure for the dynamics of a control system. Eqs. (1) and (2) describe the transformed constant variable system equations for the PMSM.

$$\frac{\mathrm{d}i_d(t)}{\mathrm{d}t} = \frac{u_d(t)}{L_d(t)} - \frac{i_d(t)R_s}{L_d(t)} + \frac{\omega_{el}(t)L_q(t)i_q(t)}{L_d(t)}. \tag{1}$$

$$\frac{\mathrm{d}i_q(t)}{\mathrm{d}t} = \frac{u_q(t)}{L_q(t)} - \frac{i_q(t)R_s}{L_q(t)} - \frac{\omega_{el}(t)L_d(t)i_d(t)}{L_q(t)} - \frac{\omega_{el}(t)\Psi_p}{L_q(t)}. \tag{2}$$

The flux correlations are given in (3) and (4) by considering the flux as

$$\psi_d(t) = L_d(t)i_d(t) + \Psi_p \tag{3}$$

and

$$\psi_q(t) = L_q(t)i_q(t). \tag{4}$$

Since a coupled system is present as described, decoupling of the voltage is performed on the basis of feedforward control. If we consider (5) and (6), we get

$$\frac{\mathrm{d}i_d(t)}{\mathrm{d}t}L_d(t) = u_d(t) - i_d(t)R_s + \omega_{el}(t)L_q(t)i_q(t) \tag{5}$$

and

$$\frac{\mathrm{d}i_q(t)}{\mathrm{d}t}L_q(t) = u_q(t) - i_q(t)R_s - \omega_{el}(t)L_d(t)i_d(t) - \omega_{el}(t)\Psi_p. \tag{6}$$

The parameter Ψ_p is defined by the main flux, which is not the total flux of the permanent magnets, but the portion that passes from rotor to stator through the air gap. The higher the flux density is, the higher is the saturation effect that occurs, especially when high torques are required. For consideration of the saturation effects, it is necessary to consider inductance as a function of the currents i_d and i_q:

$$L_{d,q} = f(i_d, i_q). \tag{7}$$

Figs. 1 and 2 show the variation of the inductances as a function of the currents i_d and i_q. These values were determined by measurement on the test bench, with the PMSM to be controlled serving as the test specimen. To go more in the depth, Figs. 1 and 2 show the curves of the current-dependent inductances L_d and L_q. A detailed measurement of the PMSM is a time-consuming undertaking, as the measurements must be as granular as possible in order to obtain a sufficiently high resolution. In addition, it is not always possible to measure up to the saturation range, for example if the PMSM is already permanently installed coupled

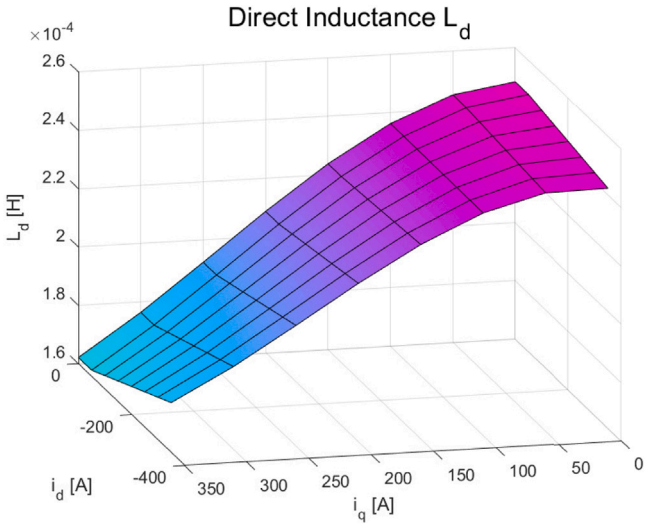

Fig. 1. Course of the characteristic field for L_d.

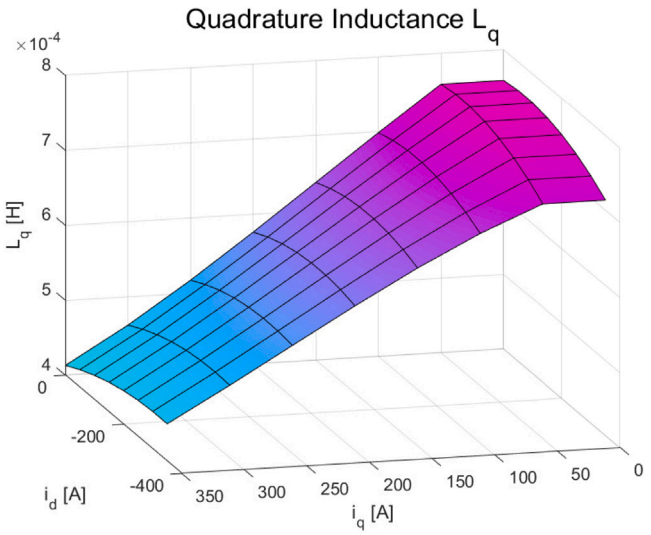

Fig. 2. Course of the characteristic field for L_q.

to a shaft. The present estimation of the saturation behavior enables a sufficiently high estimation even with a determination of only a few, in this case nine, measuring points and is therefore much more flexible. An explanation for the magnetic conditions is given in [28], where the current dependence of the inductances is illustrated. The PMSM machine equations are completed by the electrical torque equation, which can be calculated from the machine currents i_d, i_q, the main flux Ψ_p, the inductances of the PMSM L_d, L_q and the pole pair number p in (8), with

$$T(t) = \frac{3}{2} p \left\{ i_q(t)\psi_d(t) - i_d(t)\psi_q(t) \right\}. \tag{8}$$

3. MTPA and flux weakening approaches

The PMSM operates in different ranges during current control within a variable speed and torque demand range. During the constant current range, the limit of the maximum current must be maintained. At the same time, it is important to reduce the copper losses of the PMSM, which are essentially caused by the impressing of the current. Maintaining the desired torque while keeping the current limit at a minimum current amount describes a first optimization problem. If a voltage limit defined by the

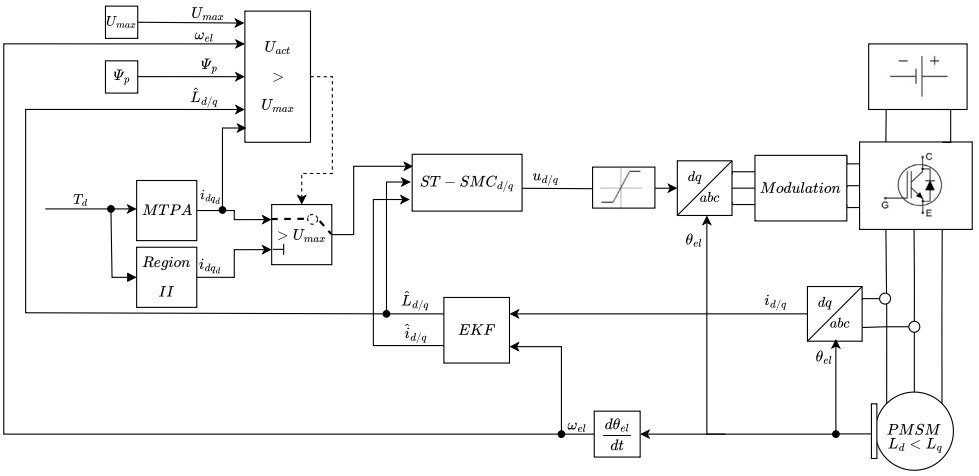

Fig. 3. The proposed control scheme.

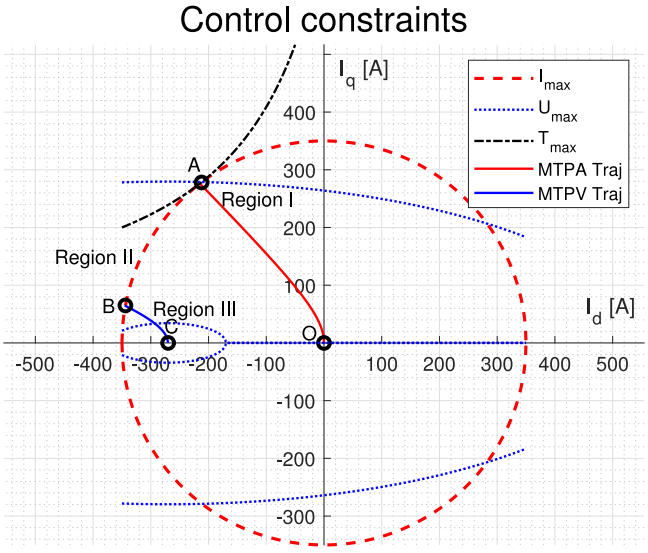

Fig. 4. Control constraints.

inverter is reached due to the increase in speed or further increase in torque, control is applied at the voltage limit. Here, taking into account the maximum allowed voltage, the maximum torque is to be set, which represents the definition of another optimization problem. As the PMSM speed increases, the induced voltage increases proportionally, leading to the need for field weakening at the voltage limit as well as the current limit. This control range is described by Region II, see set **A-B** of Figs. 4 and 5. Whether the control can take place within this region up to the maximum speed, until $i_q = 0$, clearly depends on the parameters and thus the nature of the PMSM. For PMSMs where setting the current for control at the control limit is no longer possible due to the increased reactance when the speed is increased beyond a certain range, the Region III, see set **B-C** of Figs. 4 and 5, with its control approach enters. It is the so called maximum per voltage (MTPV) optimization approach. In [29] a control strategy consisting out of MTPA and MTPV is shown without switching between both regions. Both optimization problems, the MTPA and MTPV, can be solved using a Lagrangian optimization. If both constraints, reaching current and voltage limit, are fulfilled, a combination of the two equation constraints for the maximum current as well as for the maximum voltage to solve the optimal problem is excluded due to the complexity of the solutions. In this case, the flux weakening strategy is applied, see Region II, which is represented by the set **A-B** in Figs. 4 and 5. The calculation according to Lagrange is therefore considered separately, once for the range of control at the current limit by the control rule from the MTPA and once for the range of control at the voltage limit by the control rule from the MTPV. In [30] as well as in [31], an MTPA and MTPV is carried out for an optimal control by considering the saturation conditions which occur for higher loads in the PMSM or in a synchronous reluctance machine. The long calculations for the optimal current setting can be a limitation for some controller hardware platforms, therefore [32] presented a possibility to reduce this

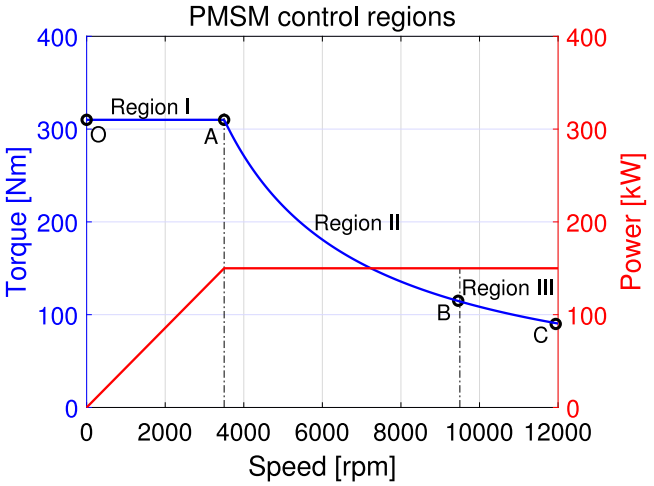

Fig. 5. Control regions.

calculation effort. The following equations present the calculation for MTPA by using the Lagrange optimization as well as for the flux weakening. Since the control was carried out in these two ranges, the MTPV is not explicitly discussed. The following remark emphasizes some aspects related to the choice of the two ranges excluding the MTPV strategy of control.

Remark 1. The consideration of two different control ranges (one in the constant torque range and the other one in the constant power range) should make it clear that the control is also capable of functioning in the range of strong non-linearities and smaller values. Since the control stability generally becomes more unstable in the constant power range, field weakening has to be active here in order to increase the speed, what reduces the motor's torque. As the torque decreases, control over the speed and load of the motor is more difficult. By showing that control is possible even in the area of the necessary field weakening, this indicates the stability of the control system.

3.1. MTPA

The PMSM operates in different regions during current control within a variable speed range. During the constant current range, Region I, the limit of the maximum current I_{max} must be maintained. At the same time, it is important to reduce the copper losses of the PMSM, which are essentially caused by the impressing of the current. The losses increase quadratically with the current and are therefore mainly load-dependent. The relationships are presented in

$$P_{loss} = i_{load}^2 R_{winding}, \tag{9}$$

where i_{load} is the load current and $R_{winding}$ is the winding resistance. Maintaining the desired torque while keeping the current limit at a minimum current amount is necessary to reduce the losses and at the same time it describes a first optimization problem. The solution is stated by the so called MTPA approach, which works in the outer control loop and defines the desired current inputs i_{dd} and i_{qd} for the torque control input. When calculating the optimization problem according to Lagrange, this corresponds to the optimization according to (8), while maintaining a maximum current amount according to

$$I_{max} \leq \sqrt{i_d(t)^2 + i_q(t)^2}, \tag{10}$$

which is defined as the equation constraint of the Lagrangian. When calculating the optimization problem according to Lagrange, it must be noted that the calculation here is usually done according to the method for the local minimum. For this purpose, the Lagrangian is set up using the objective function in (8) and the constraint from (10). This results in the following Lagrange function:

$$Lag(i_d(t), i_q(t), \Lambda) = \frac{3}{2} p \left((L_d(t) - L_q(t)) i_q(t) i_d(t) + \Psi_p i_q(t) \right) + \Lambda (I_{max}^2 - i_d(t)^2 + i_q(t)^2). \tag{11}$$

The local minimum is calculated by forming the partial derivatives of (11) according to the current components $i_d(t)$, $i_q(t)$ and Λ. The resulting equations are:

$$\frac{dLag}{di_d(t)} = \frac{3}{2} p (L_d(t) - L_q(t)) i_q(t) - 2\Lambda i_d(t), \tag{12}$$

$$\frac{dLag}{di_q(t)} = \frac{3}{2} p (\Psi_p + (L_d(t) - L_q(t)) i_d(t)) - 2\Lambda i_q(t), \tag{13}$$

and

$$\frac{d\,Lag}{d\,\Lambda} = I_{max}^2 - i_d^2(t) - i_q^2(t). \tag{14}$$

After setting (12) and (13) to zero, solving them for Λ, they can be equalized and solved for i_d, which results in the following equation:

$$i_d(t)_{1,2} = -\frac{\Psi_p \pm \sqrt{4i_q^2(t)(L_d^2(t) - L_q^2(t)) + \Psi_p^2}}{2(L_d(t) - L_q(t))}. \tag{15}$$

To obtain the torque equation with optimal current splitting, the solution where the current (15) is a minimum must be found and inserted into (8). To obtain the correct of the two solutions from (15), the singular points of the Lagrangian must be calculated with the gradient set to zero. The nature of the solutions in (15), that is, whether it is a local maximum, a local minimum or a saddle point, can then be determined by the second derivative of the Lagrangian function (11). This can be done by setting up a matrix and examining it according to the Sylvester criterion, as described in [33]. The second derivatives of the Lagrange function give:

$$\frac{d^2\,Lag}{di_d^2(t)} = -2\Lambda, \tag{16}$$

$$\frac{d^2\,Lag}{di_d(t)di_q(t)} = -\frac{3}{2}p(L_d(t) - L_q(t)), \tag{17}$$

$$\frac{d^2\,Lag}{di_q(t)di_d(t)} = -\frac{3}{2}p(L_d(t) - L_q(t)), \tag{18}$$

and

$$\frac{d^2\,Lag}{di_q^2(t)} = -2\Lambda. \tag{19}$$

The matrix then can be set up with:

$$\begin{bmatrix} \frac{d^2\,Lag}{di_d^2(t)} & \frac{d^2\,Lag}{di_d(t)di_q(t)} \\ \frac{d^2\,Lag}{di_q(t)di_d(t)} & \frac{d^2\,Lag}{di_q^2(t)} \end{bmatrix} = \begin{bmatrix} -2\Lambda & -\frac{3}{2}p(L_d(t) - L_q(t)) \\ -\frac{3}{2}p(L_d(t) - L_q(t)) & -2\Lambda \end{bmatrix}. \tag{20}$$

To check whether it is a local minimum of the Lagrangian function, all eigenvalues of the upper left minors of the matrix in (20) must be positive. For (17) and (18), a positive pole pair number is valid as well as the fact that $L_d < L_q$. To investigate when Λ becomes negative in (16) and (19),

$$\Lambda = -\frac{3p(L_d(t) - L_q(t))i_q(t)}{4i_d(t)} \tag{21}$$

has to be considered, which is obtained when the derivations in (12) and (13) are set to zero and solved for Λ. The current i_d from (15) now has to be substituted into (21). If we consider a positive motor current for i_q, a negative Λ is obtained for solution 2 in (15) and therefore the second solution with

$$i_d(t) = \frac{-\Psi_p}{2(L_d(t) - L_q(t))} - \sqrt{i_q^2(t) + \frac{\Psi_p^2}{4(L_d(t) - L_q(t))^2}} \tag{22}$$

is the right solution for considering maximum torque while obtaining constant current. To obtain the torque requirement for MTPA strategy, (8) has to be calculated with (22). This results in the following torque requirement as a function of current i_q:

$$T(i_q) = -\frac{3p\left(\frac{i_q(t)(\Psi_p + \sqrt{4i_q^2(t)(L_d(t) - L_q(t))^2 + \Psi_p^2})}{2} - i_q(t)\Psi_p\right)}{2}. \tag{23}$$

When calculating the i_q setpoint specification from (23), a 4th degree polynomial is produced with T now as the desired torque T_d:

$$i_q^4(t) + \frac{2T_d\Psi_p}{3(L_d(t) - L_q(t))^2 p} i_q(t) - \frac{(2T_d)^2}{9(L_d(t) - L_q(t))^2 p^2} = 0. \tag{24}$$

Eqs. (12) and (13) can also be equalized after solving for Λ and solved for i_q, which results in equation

$$i_q(t)_{1,2} = \pm\frac{i_d(t)\Psi_p + i_d^2(t)(L_d(t) - L_q(t))}{L_d(t) - L_q(t)}. \tag{25}$$

After searching for the local minimum by the usage of the Sylvester criterion, the correct equation is given by:

$$i_q(t) = -\frac{i_d(t)\Psi_p + i_d^2(t)(L_d(t) - L_q(t))}{L_d(t) - L_q(t)}. \tag{26}$$

The equation constraint in (14) is set to 0 and solved for i_q which leads to the quadrature current i_q under compliance with the I_{max} condition with

$$i_q(t) = \sqrt{I_{max}^2 - i_d^2(t)}. \tag{27}$$

Equating both equations of i_q, (26) as well as (27), and solving for i_d, gives the specification for the field-forming current i_d under compliance with the I_{max} condition with

$$i_d(t) = \frac{-\Psi_p}{4(L_d(t) - L_q(t))} - \sqrt{\frac{I_{max}^2}{2} + \frac{\Psi_p^2}{16(L_d(t) - L_q(t))^2}}. \tag{28}$$

To select the correct solution from the four solutions resulting for i_q out of (24), several constraints have to be performed in the solution approach. The desired solution must be real and positive for i_q in motor operation. The operating constraint for i_q is given by (27). To better illustrate the constraints on the selection of set currents for i_d and i_q, see Region I characterized by set **O-A** of Figs. 4 and 5. Here I_{max} describes the circle with fixed radius of the maximum usable current for reaching maximum torque T_{max}. I_{max} is divided into i_d and i_q components, according to (10), which also is the equation constraint of the Lagrangian for the MTPA. The intersection of the MTPA trajectory in Fig. 4 gives the maximum torque by maintaining minimum current in point A. For controlling the torque while maintaining the minimum required current, the respective intersection point with the desired torque can be used along the MTPA trajectory to obtain the specification for i_d as well as i_q. In the global calculation of the optimum, which means that the optimization problem of MTPA as well as MTPV are considered in a joint solution, as it can be calculated using the Bellman principles of optimization approach, a constraint arises for the control condition of i_q as well as for i_d. These constraints do not arise when a suboptimal solution is considered with the calculation by the usage of the Lagrangian for MTPA and the constraints for the flux weakening control. Therefore, and due to the shorter solution of the suboptimal, the use of the results of the calculation of the suboptimals is done.

3.2. Flux weakening

If a voltage limit defined by the inverter is reached due to the increase in speed or further increase in torque, the control is applied additionally or even exclusively at the voltage limit. From this point, field weakening is necessary to increase the speed of the PMSM. A control is therefore carried out in Region II, see Fig. 4, at the current as well as at the voltage limit. The control is described by flux limit

$$\psi^2 = \psi_d^2 + \psi_q^2, \tag{29}$$

respectively the voltage limit

$$\frac{U_{max}^2}{\omega_{el}^2(t)} = \left(\Psi_p + L_d(t) i_d(t)\right)^2 + \left(L_q(t) i_q(t)\right)^2. \tag{30}$$

If (30) is resolved for the current division according to i_d, it can be seen that a maximum achievable speed exists:

$$i_d(t) = -\frac{\Psi_p}{L_d(t)} \pm \frac{1}{L_d(t)} \sqrt{\frac{U_{max}^2}{\omega_{el}^2(t)} - (L_q(t) i_q(t))^2}. \tag{31}$$

If the speed is too high, the root in (32) becomes negative. The maximum speed is therefore reached as soon as the term below the root becomes zero. The resulting point is also called the short-circuit point. The coordinates for the short-circuit point as the origin of the voltage boundary ellipses, as shown in Fig. 4, can be calculated as follows:

$$i_d(t) = -\frac{\Psi_p}{L_d(t)}; i_q(t) = 0. \tag{32}$$

To continue the control at the current limit as well as at the voltage limit, that is in Region II, (30) is solved for i_d and replaced in (8), what leads to

$$T_{fw} = \frac{3}{2} p \left(\Psi_p i_q(t) + \frac{L_d(t) - L_q(t)}{L_d(t)} A i_q(t) \right), \tag{33}$$

with

$$A = -\Psi_p \pm \sqrt{\frac{U_{max}^2}{\omega_{el}^2(t)} - L_q^2(t) i_q^2(t)}.$$

Solving (33) for i_q results in a 4th order polynomial. To obtain the correct solution for the currents i_q and thus also i_d, several criteria must be fulfilled. The solution must be within the defined limits, be real and $i_q > 0$ for motor operation. So as to summarize, control in Region II takes place for the existence of two limits, as control in Region I and III exists for current or voltage limit. In principle, the control can be continued up to the maximum speed in Region II. However, as to be seen in (31), for a defined speed control at the current limit is no longer possible, resulting in only one limit range prevailing. When the short circuit point of (32) lies outside the circle of the maximum current amount, the control in Region II is possible for the whole speed amount. In case the short circuit point of (32) lies inside this circle, the higher speeds are achieved by a different control, the MTPV approach, that takes these into account.

4. A decoupling ST-SMC approach for PMSM

Decoupling control is a widely used control technique in practice. Accurate and fast parameter estimation is extremely important for the operation and control of PMSMs. Recently in [34] a parameter decoupling estimation method based on multi-state measurement was proposed to analyze and estimate parameters of the machines, such as inductances. More recently also in [1] a decoupling based on feedforward action has been applied to simplify the identification algorithm for estimating the inductances in a PMSM. The idea in this paper is to use the two input voltages u_d and u_q to obtain the two noninteracting dynamics d and q using a robust control method based on the definition of two decoupled floating manifolds, s_d and s_q. SMC is the term used to describe a nonlinear control strategy that applies a discontinuous signal to change the dynamics of a system. SMC systems are divided into two different phases, the so-called reaching phase and the sliding phase. During the reaching phase, the SMC attempts to bring the system to the sliding surface. Once the sliding phase is reached, the SMC tries to hold this system state over the sliding phase with the help of a switching function. The control signal of the SMC is a discontinuous signal, which makes it difficult to use within the electrical control loop. The application of the ST-SMC therefore has the ability to combine the advantages of the SMC while eliminating the disadvantage by using a continuous control signal [35]. By deriving the sliding function $s(t) \to 0$, a linear function is obtained. To recall some fundamental background information, the following remark is proposed

Remark 2. The presented remark is in agreement with [8,9]. In particular, the authors of [9] used the same following property in their Eq. (36) in the context of ST-SMC:

$$\int_0^t \operatorname{sgn}(s(\tau))d\tau = \operatorname{sgn}(s(t)) \int_0^t d\tau, \tag{34}$$

where $s(t)$ is the sliding surface. This property is based on the equivalent control part and the construction of equivalent dynamics, see [36] and more directly in [37] on page 283–286, where it is clarified how $\dot{s}(t) = 0$ and $s(t) = 0$ is guaranteed even with imperfect switching control. In fact, the two correcting parts of the controller guarantee the "average residence" of the trajectory of the surface with $\dot{s}(t) = 0$ and $s(t) = 0$ since the control switching is 'infinitely' fast.

Remark 3. If we examine the theoretically infinitely fast switching processes in more detail using the following considerations, we see that on the surface $\dot{s}(t) = 0$ and $s(t) = 0$ and that therefore (35) can be applied. If we consider t_i time points with $m = 1, 2, \dots, n$, in which the trajectory passes through the sliding surface, then the following expression

$$\int_{t_i^-}^{t_i^+} \operatorname{sgn}(s(\tau))d\tau = 0 \tag{35}$$

can be proven, where t_i^- and t_i^+ indicate the infinitesimal time before and after the intersection with the surface at time t_i. In fact, with the help of integration by parts, then is

$$\int_{t_i^-}^{t_i^+} \operatorname{sgn}(s(\tau))d\tau = \operatorname{sgn}(s(\tau))\tau\Big|_{t_i^-}^{t_i^+} - \int_{t_i^-}^{t_i^+} \delta(\tau - t_i)\dot{s}(\tau)d\tau. \tag{36}$$

If $t_i^- \to t_i^+ \to t_i$, then $\operatorname{sgn}(s(\tau))\tau\Big|_{t_i^-}^{t_i^+} \to 0$ applies where the presence of the pulse indicates that the switching is infinitely fast at time t_i. Considering the second part of (36) and integrating it by parts, then

$$1 \times \int_{t_i^-}^{t_i^+} \delta(\tau - t_i)\dot{s}(\tau)d\tau = \tau \int_{t_i^-}^{t_i^+} \delta(\tau - t_i)\dot{s}(\tau)d\tau\Big|_{t_i^-}^{t_i^+} - \int_{t_i^-}^{t_i^+} 1 \times \Big(\int_{t_i^-}^{t_i^+} \delta(\tau - t_i)\dot{s}(\tau)d\tau\Big)d\zeta \tag{37}$$

and using the shifting property of the impulse, then it is

$$\tau \int_{t_i^-}^{t_i^+} \delta(\tau - t_i)\dot{s}(\tau)d\tau\Big|_{t_i^-}^{t_i^+} - \int_{t_i^-}^{t_i^+} 1 \times \Big(\int_{t_i^-}^{t_i^+} \delta(\tau - t_i)\dot{s}(\tau)d\tau\Big)d\zeta = \tau\dot{s}(t_i)\Big|_{t_i^-}^{t_i^+} - \tau\dot{s}(t_i)\Big|_{t_i^-}^{t_i^+} = 0. \tag{38}$$

This indicates that if the switching occurs infinitely fast at t_i, then expression (35) is true and therefore also on the surface is $\dot{s}(t) = 0$ and $s(t) = 0$. For further analysis, see [36].

Proposition 1. *Considering the model for the PMSM described in (1) and (2), two control laws are obtained that globally stabilize asymptotically the system around the reference currents i_{dd} and i_{qd} assuming that disturbances and model uncertainties of the d and q dynamics, φ_d and φ_q are Lipschitz functions and such that $|\dot{\varphi}_d| \leq \delta_d$ and $|\dot{\varphi}_q| \leq \delta_q$ with δ_d and δ_q are real numbers.*

Proof. The errors are defined in the following way:

$$e_q(t) = i_{dd}(t) - i_d(t) \tag{39}$$

and

$$e_d(t) = i_{qd}(t) - i_q(t), \tag{40}$$

and therefore the set up sliding surfaces in (41) and (42):

$$s_d(t) = e_d(t) + k_1 \int_0^t e_d(\tau) d\tau - e_\tau(0^-) \tag{41}$$

and

$$s_q(t) = e_q(t) + k_2 \int_0^t e_q(\tau) d\tau - e_\tau(0^-). \tag{42}$$

It is worth mentioning here that the terms $e_{id}(0)$ and $e_{iq}(0)$ bring the phase to be reached to zero regardless of the initial values of the currents $i_d(0)$ and $i_q(0)$. To obtain the state on the sliding surface $s = 0$, the currents i_d and i_q must converge exponentially to their reference values. The parameters k_1 as well as k_2 thereby form the positive gains for the dynamic stability, with $e_\tau(0^-) = 0$. The Lyapunov function

$$V(t) = \frac{1}{2} s_q^2(t) + \frac{1}{2} s_d^2(t) \tag{43}$$

and its derivation

$$\dot{V}(t) = s_q(t)\dot{s}_q(t) + s_d(t)\dot{s}_d(t), \tag{44}$$

where $s_d(t)$ and $s_q(t)$ are the limits for the stationary system with the derivations

$$\dot{s}_d(t) = \dot{e}_d(t) + k_1 e_d(t) = 0 \tag{45}$$

and

$$\dot{s}_q(t) = \dot{e}_q(t) + k_2 e_q(t) = 0. \tag{46}$$

By inserting terms $\dot{s_d}$ and $\dot{s_q}$ we get

$$\dot{V}(t) = s_q(t) \left[\frac{di_{qd}(t)}{dt} - \frac{di_q(t)}{dt} + k_1 \left(i_{qd}(t) - i_q(t) \right) + s_d(t) \left(\frac{di_{dd}(t)}{dt} - \frac{di_d(t)}{dt} \right) + k_2 \left(i_{dd}(t) - i_d(t) \right) \right]. \tag{47}$$

Taking into account (1) and (2), then the following expressions are obtained:

$$\dot{V}_{sd}(t) = s_d(t) \left[\frac{di_{dd}(t)}{dt} - \frac{u_d(t)}{L_d(t)} + \frac{i_d(t) R_s}{L_d(t)} - \frac{\omega_{el}(t) L_q(t) i_q(t)}{L_d(t)} + k_2 \left(i_{dd}(t) - i_d(t) \right) \right] \tag{48}$$

and

$$\dot{V}_{sq}(t) = s_q(t) \left[\frac{di_{qd}(t)}{dt} - \frac{u_q(t)}{L_q(t)} + \frac{i_q(t) R_s}{L_q(t)} + \frac{\omega_{el}(t) L_d(t) i_d(t)}{L_q(t)} + \frac{\omega_{el}(t) \Psi_p}{L_q(t)} + k_1 \left(i_{qd}(t) - i_q(t) \right) \right], \tag{49}$$

where

$$\dot{V}(t) = \dot{V}_{sd}(t) + \dot{V}_{sq}(t). \tag{50}$$

Calculating the equivalent inputs u_d and u_q which realize $\dot{s}_d(t) = 0$ and $\dot{s}_q(t) = 0$ respectively through (48) and (49), the following expressions are obtained of the ST-SMC controller:

$$u_{ed}(t) = \hat{L}_d(t) \left[\frac{di_{dd}(t)}{dt} + \frac{R_s \hat{i}_d(t)}{\hat{L}_d(t)} - \frac{\omega_{el}(t) \hat{L}_q(t) \hat{i}_d(t)}{\hat{L}_d(t)} + k_1 (i_{dd}(t) - \hat{i}_d(t)) \right] \tag{51}$$

and

$$u_{eq}(t) = \hat{L}_q(t) \left[\frac{di_{qd}(t)}{dt} + \frac{R_s \hat{i}_q(t)}{\hat{L}_q(t)} + \frac{\omega_{el}(t) \hat{L}_d(t) \hat{i}_d(t)}{\hat{L}_q(t)} + \frac{\omega_{el}(t) \Psi_p}{\hat{L}_q(t)} + k_2 \left(i_{qd}(t) - \hat{i}_q(t) \right) \right], \tag{52}$$

where $\hat{i}_d$, $\hat{i}_q$, $\hat{L}_d$ and $\hat{L}_q$ are the states estimated by EKF. In fact, if (51) and (52) are inserted into (48) and into (49) respectively, then $\dot{V}_{sd} = 0$ and $\dot{V}_{sq} = 0$ are obtained. To obtain $\dot{V}_{sd} < 0$ and $\dot{V}_{sq} < 0$ it is enough to consider the following control law in accordance with [37]:

$$u_d(t) = u_{ed}(t) + u_{\mathrm{dcor}}(t) \tag{53}$$

and

$$u_q(t) = u_{eq}(t) + u_{\mathrm{qcor}}(t). \tag{54}$$

So as already mentioned, the controller output of the ST-SMC contains two parts. The equivalent and the corrective part. The corrective parts are given with:

$$u_{\mathrm{dcor}}(t) = \sqrt{U_d} \sqrt{|s_d(t)|} \operatorname{sgn}(s_d(t)) + \xi(t) \tag{55}$$

$$\dot{\xi}_d(t) = W_d \operatorname{sgn}(s_d(t)) \tag{56}$$

and

$$u_{\text{qcor}}(t) = \sqrt{U_q}\sqrt{|s_q(t)|}\,\text{sgn}(s_q(t)) + \xi_q(t) \tag{57}$$

$$\dot{\xi}_q(t) = W_q\,\text{sgn}(s_q(t)). \tag{58}$$

The parameters U_d, U_q, W_d and W_q represent positive constants which, in order to ensure asymptotic stability, are calculated according to [8,9], $W_d > \delta_d$ and $W_q > \delta_q$, where $\delta_{(.)}$ is the upper bound of the derivative of the disturbance. In fact, considering the model uncertainties and disturbances $\varphi_d(t)$ and $\varphi_q(t)$, through the two equivalent parts u_{ed} and u_{eq} the following expression from (47) is obtained:

$$\begin{aligned}\dot{V}(t) &= s_d(t)[-\sqrt{U_d}\sqrt{|s_d(t)|}\,\text{sgn}(s_d(t)) - \xi_d(t) + \varphi_d(t)] + s_q(t)[-\sqrt{U_q}\sqrt{|s_q(t)|}\,\text{sgn}(s_q(t)) - \xi_q(t) + \varphi_q(t)] \\ &\leq s_d(t)[-\xi_d(t) + \varphi_d(t)] + s_q(t)[-\xi_q(t) + \varphi_q(t)].\end{aligned} \tag{59}$$

If the following transformations are considered:

$$\chi_d(t) = -W_d \int_0^t \text{sgn}(s_d(\tau))d\tau + \varphi_d(t) - \varphi_d(0) \tag{60}$$

and

$$\chi_q(t) = -W_q \int_0^t \text{sgn}(s_q(\tau))d\tau + \varphi_q(t) - \varphi_q(0), \tag{61}$$

then expression (59) becomes as follows:

$$\dot{V}(t) \leq s_d(t)[\chi_d(t) + \varphi_d(0)] + s_q(t)[\chi_q(t) + \varphi_q(0)] \tag{62}$$

because

$$\varphi_{(.)}(t) - \varphi_{(.)}(0) = \int_0^t \dot{\varphi}_{(.)}(\tau)d\tau. \tag{63}$$

From (60), (61) and (62), the following expression can be obtained:

$$\dot{V}(t) \leq s_d(t)[-W_d \int_0^t \text{sgn}(s_d(\tau))d\tau + \int_0^t \dot{\varphi}_d(\tau)d\tau] + s_q(t)[-W_q \int_0^t \text{sgn}(s_q(\tau))d\tau + \int_0^t \dot{\varphi}_q(\tau)d\tau]. \tag{64}$$

It is straightforward to see that if $W_d > |\dot{\varphi}_d| \leq \delta_d$ and $W_q > |\dot{\varphi}_q| \leq \delta_q$ then $\dot{V}(t) \leq 0$. In fact, in accordance with the recalls of Remarks 2 and 3 based on fundamentals for a sliding surface $s(t)$ of [36,37], also as shown in [8,9] being

$$\int_0^t \text{sgn}(s(\tau))d\tau = \text{sgn}(s(t)) \int_0^t d\tau \tag{65}$$

and being W_d and W_q constant parameters, then (64) can be written as follows:

$$\dot{V}(t) \leq s_d(t)[-\,\text{sgn}(s_d(t)) \int_0^t W_d d\tau + \int_0^t \dot{\varphi}_d(\tau)d\tau] + s_q(t)[-\,\text{sgn}(s_q(t)) \int_0^t W_q d\tau + \int_0^t \dot{\varphi}_q(\tau)d\tau] \tag{66}$$

and it follows that

$$\dot{V}(t) \leq -|s_d(t)| \int_0^t W_d d\tau + s_d(t) \int_0^t \dot{\varphi}_d(\tau)d\tau - |s_q(t)| \int_0^t W_q d\tau + s_q(t) \int_0^t \dot{\varphi}_q(\tau)d\tau \tag{67}$$

and thus

$$\dot{V}(t) \leq -|s_d(t)| \int_0^t W_d d\tau + \left| s_d(t) \int_0^t \dot{\varphi}_d(\tau)d\tau \right| - |s_q(t)| \int_0^t W_q d\tau + \left| s_q(t) \int_0^t \dot{\varphi}_q(\tau)d\tau \right|. \tag{68}$$

Applying the property of the absolute value with respect to the product of two functions, it follows:

$$\dot{V}(t) \leq -|s_d(t)| \int_0^t W_d d\tau + |s_d(t)| \left| \int_0^t \dot{\varphi}_d(\tau)d\tau \right| - |s_q(t)| \int_0^t W_q d\tau + |s_q(t)| \left| \int_0^t \dot{\varphi}_q(\tau)d\tau \right|. \tag{69}$$

If the property of the absolute value with respect to the integral function is applied, then it follows:

$$\dot{V}(t) \leq -|s_d(t)| \int_0^t W_d d\tau + |s_d(t)| \int_0^t |\dot{\varphi}_d(\tau)|d\tau - |s_q(t)| \int_0^t W_q d\tau + |s_q(t)| \int_0^t |\dot{\varphi}_q(\tau)|d\tau \tag{70}$$

and from (70), then

$$\dot{V}(t) \leq |s_d(t)| \int_0^t \left(|\dot{\varphi}_d(\tau)| - W_d \right) d\tau + |s_q(t)| \int_0^t \left(|\dot{\varphi}_q(\tau)| - W_q \right) d\tau \tag{71}$$

and from (71), then if $W_d > |\dot{\varphi}_d| \leq \delta_d$ and $W_q > |\dot{\varphi}_q| \leq \delta_q$ then $\dot{V}(t) < 0$. □

Remark 4. The parameters $U_{(.)}$ and $W_{(.)}$ are two positive constants that should be manually tuned to be large enough to ensure a good performance. A good rule of thumb is to set $W_{(.)} \approx 1.1U_{(.)}$ for a generally good dynamic tuning, as in [38,39] or in [40]. It is well known that ST-SMC, in order to obtain asymptotic convergence, does not require the a priori knowledge of the upper bound of the perturbations and/or model uncertainties, but it is only necessary to assume that the derivative of the perturbations and model uncertainties are bounded. However, in case a finite time convergence is requested, then the a priori knowledge of the upper bound of the model uncertainties and disturbance is required as a sufficient condition, see [41].

5. EKF for saturated conditions

5.1. Calculation of the bivariate polynomial

To calculate a better model for the inductance parameter estimation in the EKF, a bivariate polynomial with help of some measured setpoints is calculated and given into the EKF. The advantage is the better estimation in a saturated region, due to the better model quality. In (72) the general form of the bivariate polynomial is given by

$$f := n \rightarrow \sum_{j=0}^{n} \Big(\sum_{i=0}^{m} a_{i,j}\, x^i y^j \Big). \tag{72}$$

To build the model for the EKF, the coefficients must be calculated using $\boldsymbol{\Theta}_d$ and $\boldsymbol{\Theta}_q$ in (73) for the bivariate polynomial of the current-dependent inductance.

$$\begin{bmatrix} \boldsymbol{\Theta}_d \\ \boldsymbol{\Theta}_q \end{bmatrix} = \begin{bmatrix} \mathbf{X}_{d/q}^T \mathbf{X}_{d/q} \\ \mathbf{X}_{d/q}^T \mathbf{X}_{d/q} \end{bmatrix}^{-1} \begin{bmatrix} \mathbf{X}_{d/q}^T \mathbf{L}_{dD} \\ \mathbf{X}_{d/q}^T \mathbf{L}_{qD} \end{bmatrix}. \tag{73}$$

The calculation of $\mathbf{X}_{d/q}$ is done using the current vectors $\mathbf{I_d}$ and $\mathbf{I_q}$:

$$\mathbf{I_d} = \begin{bmatrix} -350 & -150 & 0 \end{bmatrix} \tag{74}$$

and

$$\mathbf{I_q} = \begin{bmatrix} 0 & 200 & 350 \end{bmatrix}. \tag{75}$$

After calculating the current vectors, the matrix for $\mathbf{X}_{d/q}$ is calculated:

$$\mathbf{X}_{d/q} = \begin{bmatrix} I_q(1)\mathbf{I_d^T} & \mathbf{I_d^T} & I_q(1)\mathbf{I}_{3\times1} & \mathbf{I}_{3\times1} \\ I_q(2)\mathbf{I_d^T} & \mathbf{I_d^T} & I_q(2)\mathbf{I}_{3\times1} & \mathbf{I}_{3\times1} \\ I_q(3)\mathbf{I_d^T} & \mathbf{I_d^T} & I_q(3)\mathbf{I}_{3\times1} & \mathbf{I}_{3\times1} \end{bmatrix}. \tag{76}$$

By adapting the example in (72) the following structures for dependence of the currents i_d and i_q are obtained:

$$\begin{bmatrix} L_q(1,1) \\ L_q(1,2) \\ L_q(1,3) \end{bmatrix} = \begin{bmatrix} \Theta_q(1)I_d(1)I_q(1) + \Theta_q(2)I_d(1) + \Theta_q(3)I_q(1) + \Theta_q(4) \\ \Theta_q(1)I_d(1)I_q(2) + \Theta_q(2)I_d(1) + \Theta_q(3)I_q(2) + \Theta_q(4) \\ \Theta_q(1)I_d(1)I_q(3) + \Theta_q(2)I_d(1) + \Theta_q(3)I_q(3) + \Theta_q(4) \end{bmatrix}. \tag{77}$$

In dependence of the current i_d the following structure is obtained:

$$\begin{bmatrix} L_d(1,1) \\ L_d(2,1) \\ L_d(3,1) \end{bmatrix} = \begin{bmatrix} \Theta_d(1)I_d(1)I_q(1) + \Theta_d(2)I_d(1) + \Theta_d(3)I_q(1) + \Theta_d(4) \\ \Theta_d(1)I_d(2)I_q(1) + \Theta_d(2)I_d(2) + \Theta_d(3)I_q(2) + \Theta_d(4) \\ \Theta_d(1)I_d(3)I_q(1) + \Theta_d(2)I_d(3) + \Theta_d(3)I_q(3) + \Theta_d(4) \end{bmatrix}. \tag{78}$$

Figs. 6 and 7 represent the inductances L_d and L_q calculated in dependence for its current vectors $\mathbf{I_d}$ and $\mathbf{I_q}$. The inductances L_d and L_q then can be written in (79) and (80) with

$$L_d(t) = \Theta_d(1)i_d(t)i_q(t) + \Theta_d(2)i_d(t) + \Theta_d(3)i_q(t) + \Theta_d(4) \tag{79}$$

and

$$L_q(t) = \Theta_q(1)i_d(t)i_q(t) + \Theta_q(2)i_q(t) + \Theta_q(3)i_d(t) + \Theta_q(4). \tag{80}$$

A good explanation of the calculation of the bivariate polynomial for the PMSM is given in [42].

6. EKF for estimation of inductance

The EKF offers the possibility to estimate the parameters of a nonlinear system by linearizing the model functions by a Taylor series. A basic background shall be given of the proposed EKF for better understanding of the implemented structure in the following text. A good overview as well as a tutorial for the EKF background and the implementation of different KFs is given in [43].

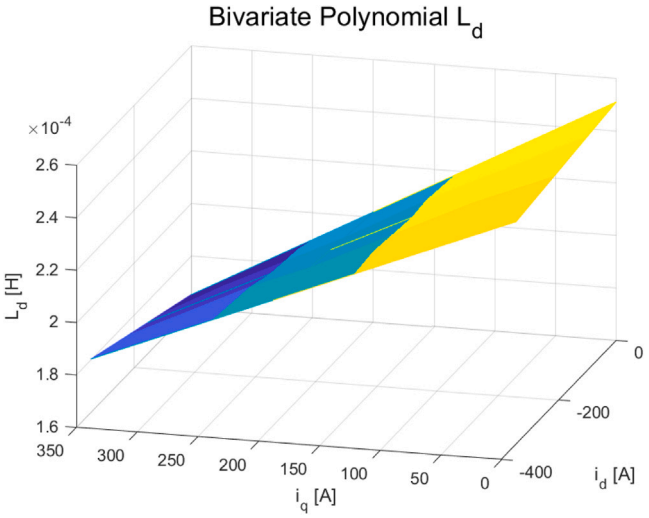

Fig. 6. Calculated bivariate polynomial L_d.

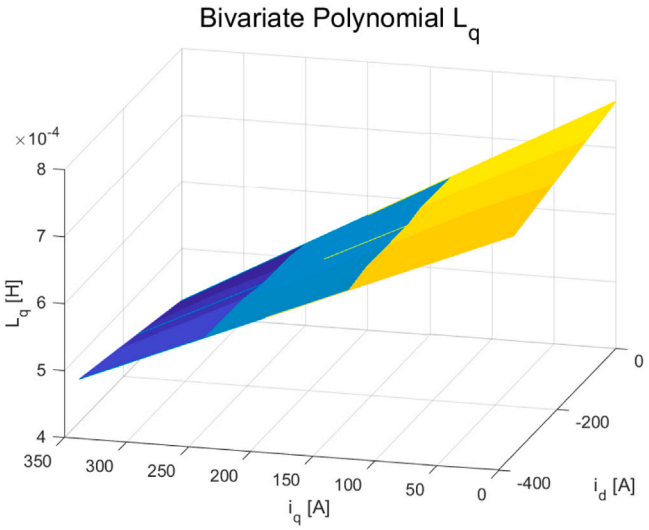

Fig. 7. Calculated bivariate polynomial L_q.

6.1. EKF background

In [44], the a priori estimation of the state can be seen and written down as follows:

$$\hat{x}^{-}(k+1) = f(\hat{x}(k), u(k), w(k)), \quad k \in \mathbb{N} \tag{81}$$

with the function $f(\hat{x}, u, w)$ that stands for a nonlinear field which is used to model a system to be considered. After calculating the Jacobian matrix J, the a priori error covariance of the state prediction can be calculated as follows:

$$P^{-}(k+1) = J(k+1)P(k)J(k+1)^{T} + Q, \tag{82}$$

with P representing the a posteriori error covariance matrix at the previous step k. The covariance matrix of the process noise is given with matrix Q and can be interpreted as the quantification of the uncertainty of the model. The reliability of the model can be seen from the values of the trace in the matrix, that is, the smaller the values, the higher the reliability of the model. Last but not least, the Kalman gain K has to be calculated. The Kalman gain is used as minimization for the a posteriori error covariance and is set up with

$$K(k+1) = P^{-}(k+1)H^{T}(HP^{-}(k+1)H^{T} + R_w)^{-1}. \tag{83}$$

The matrix R_w is the covariance matrix for the measurement noise. From these descriptions, it can be seen that the matrices Q and R_w represent the tuning parameters of the system. The output Jacobian matrix is defined by the usage of matrix H. It is used as an indication for the EKF algorithm to define which state serves as the measurement. Considering the a posteriori estimation, (84) has to be considered.

$$\hat{x}(k+1) = \hat{x}^{-}(k+1) + K(k+1)(z(k+1) - H\hat{x}^{-}(k+1)), \tag{84}$$

with

$$z_k(k+1) = x(k+1) + v(k+1), \tag{85}$$

where z_k gives the data that is measured and in which the vector signal v gives the measured white Gaussian noise. As defined before, the vector signal v is associated with the sensoring system and assumed to be independent of process white Gaussian noise. The a posteriori estimation of the error covariance is given below with (86)

$$P(k+1) = (I - K(k+1)H)P^{-}(k+1). \tag{86}$$

When considering the combined extended Kalman filter (CEKF), it has to be kept in mind, that it divides the states to be estimated in two models, one for the estimations of the electrical states like currents and inductances (i_d, i_q, L_d and L_q) and another one for the estimation of the mechanical states like $load$, θ_r and ω_r. An example for the usage of the CEKF in another context is given in [45].

6.2. The proposed CEKF

In the proposed analysis, the operating point of the motor can also be in the saturation region and thus the estimation of L_d and L_q is of particular interest in the optimization procedure and also for the decoupling control realized with the equivalent part of the ST-SMC. The electrical model, obtained with a forward Euler discretization and sampling time T_s is described by the following equations for the currents in (1) and (2):

$$\tilde{i_d}(k) = \frac{i_d(k+1) - i_d(k)}{Ts} = \frac{u_d(k)}{L_d(k)} - \frac{i_d(k)R_s}{L_d(k)} + \frac{\omega_{el}(k)L_q(k)i_q(k)}{L_d(k)}, \tag{87}$$

$$\tilde{i_q}(k) = \frac{i_q(k+1) - i_q(k)}{Ts} = \frac{u_q(k)}{L_q(k)} - \frac{i_q(k)R_s}{L_q(k)} - \frac{\omega_{el}(k)L_d(k)i_d(k)}{L_q(k)} - \frac{\omega_{el}(k)\Psi_p}{L_q(k)}. \tag{88}$$

The calculations of the inductances L_d and L_q are given in (79) and (80) and their discrete differentiations are as follows:

$$\frac{L_d(k+1) - L_d(k)}{Ts} = \Theta_d(1)i_q(k)\tilde{i_d}(k) + \Theta_d(1)i_d(k)\tilde{i_q}(k) + \Theta_d(2)\tilde{i_d}(k) + \Theta_d(3)\tilde{i_q}(k) \tag{89}$$

and

$$\frac{L_q(k+1) - L_q(k)}{Ts} = \Theta_q(1)i_q(k)\tilde{i_d}(k) + \Theta_q(1)i_d(k)\tilde{i_q}(k) + \Theta_q(2)\tilde{i_d}(k) + \Theta_q(3)\tilde{i_q}(k). \tag{90}$$

The estimation of the a priori states $\hat{x}^{-}(k+1)$ is represented in (91). Therefore (87) and (88) for the discrete derivatives of the currents i_d and i_q as well as (89) and (90) for the discrete derivatives of the inductances L_d and L_q are used.

$$\begin{bmatrix} \hat{i}_d^{-}(k+1) \\ \hat{i}_q^{-}(k+1) \\ \hat{L}_d^{-}(k+1) \\ \hat{L}_q^{-}(k+1) \end{bmatrix} = \begin{bmatrix} \hat{i}_d(k) - \frac{T_s R_s \hat{i}_d(k)}{\hat{L}_d(k)} + \frac{T_s p\omega_r(k)\hat{i}_q(k)\hat{L}_q(k)}{\hat{L}_d(k)} + \frac{T_s u_d(k)}{\hat{L}_d(k)} \\ \hat{i}_q(k) - \frac{T_s(-p)\omega_r(k)\hat{i}_d(k)\hat{L}_d(k)}{\hat{L}_q(k)} - \frac{T_s R_s \hat{i}_q(k)}{\hat{L}_q(k)} + \frac{T_s u_q(k)}{\hat{L}_q(k)} - \frac{T_s \Psi_p p\omega_r(k)}{\hat{L}_q(k)} \\ \hat{L}_d(k) + T_s\left(\Theta_d(1)\hat{i}_q(k)\tilde{i_d}(k) + \Theta_d(1)\hat{i}_d(k)\tilde{i_q}(k) + \Theta_d(2)\tilde{i_d}(k) + \Theta_d(3)\tilde{i_q}(k)\right) \\ \hat{L}_q(k) + T_s\left(\Theta_q(1)\hat{i}_d(k)\tilde{i_q}(k) + \Theta_q(1)\hat{i}_q(k)\tilde{i_d}(k) + \Theta_q(2)\tilde{i_d}(k) + \Theta_q(3)\tilde{i_q}(k)\right) \end{bmatrix}. \tag{91}$$

In the EKF, the discrete nonlinear system equations in (91) are used for estimating the a priori states $\hat{x}^{-}(k+1)$ in the prediction step. From the data sheet, the initial values $\hat{x}^{+}(0)$ can be obtained for the inductances L_d and L_q, while a value other than 0 can be written for the initial values of the currents i_d and i_q. The estimation of the a priori states $\hat{x}^{-}(k+1)$, that is, the predicted states, is performed in the EKF using the a posteriori estimate $\hat{x}^{+}(k)$ of the last iteration. The Jacobian matrix, calculated at the a posteriori corrected states, is used to linearize the nonlinear system equations of the electrical model in the estimation process of the EKF.

$$J_f(k+1) = \begin{bmatrix} \frac{\partial \hat{i}_d^{-}(k+1)}{\partial \hat{i}_d(k)} & \frac{\partial \hat{i}_d^{-}(k+1)}{\partial \hat{i}_q(k)} & \frac{\partial \hat{i}_d^{-}(k+1)}{\partial \hat{L}_d(k)} & \frac{\partial \hat{i}_d^{-}(k+1)}{\partial \hat{L}_q(k)} \\ \frac{\partial \hat{i}_q^{-}(k+1)}{\partial \hat{i}_d(k)} & \frac{\partial \hat{i}_q^{-}(k+1)}{\partial \hat{i}_q(k)} & \frac{\partial \hat{i}_q^{-}(k+1)}{\partial \hat{L}_d(k)} & \frac{\partial \hat{i}_q^{-}(k+1)}{\partial \hat{L}_q(k)} \\ \frac{\partial \hat{L}_d^{-}(k+1)}{\partial \hat{i}_d(k)} & \frac{\partial \hat{L}_d^{-}(k+1)}{\partial \hat{i}_q(k)} & \frac{\partial \hat{L}_d^{-}(k+1)}{\partial \hat{L}_d(k)} & \frac{\partial \hat{L}_d^{-}(k+1)}{\partial \hat{L}_q(k)} \\ \frac{\partial \hat{L}_q^{-}(k+1)}{\partial \hat{i}_d(k)} & \frac{\partial \hat{L}_q^{-}(k+1)}{\partial \hat{i}_q(k)} & \frac{\partial \hat{L}_q^{-}(k+1)}{\partial \hat{L}_d(k)} & \frac{\partial \hat{L}_q^{-}(k+1)}{\partial \hat{L}_q(k)} \end{bmatrix}. \tag{92}$$

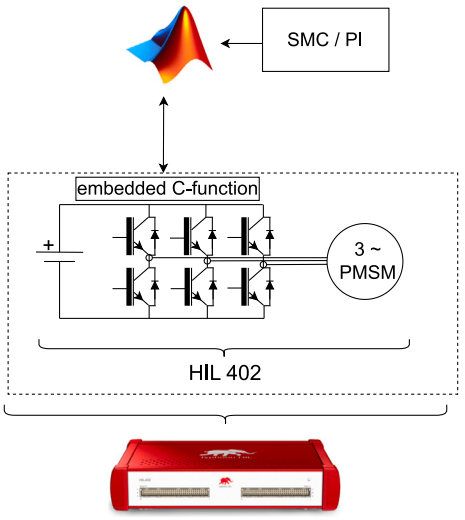

Fig. 8. HIL Setup for SMC and PI control structure.

After calculating the Jacobian matrix by using the estimation results of the last iteration, we get the following 4×4 matrix for the electrical system:

$$J_f(k+1) = \begin{bmatrix} 1 - T_s \frac{R_s}{\hat{L}_d(k)} & T_s \omega_{el}(k) \frac{\hat{L}_q(k)}{\hat{L}_d(k)} & J_{f_{13}} & T_s \omega_{el}(k) \frac{\hat{i}_q(k)}{\hat{L}_d(k)} \\ -T_s \omega_{el}(k) \frac{\hat{L}_d(k)}{\hat{L}_q(k)} & 1 - T_s \frac{R_s}{\hat{L}_q(k)} & -T_s \omega_{el}(k) \frac{\hat{i}_d(k)}{\hat{L}_q(k)} & J_{f_{24}} \\ J_{f_{31}} & J_{f_{32}} & J_{f_{33}} & J_{f_{34}} \\ J_{f_{41}} & J_{f_{42}} & J_{f_{43}} & J_{f_{44}} \end{bmatrix}. \tag{93}$$

The elements $J_{f_{13}}$ and $J_{f_{24}}$ to $J_{f_{44}}$ are reported in the appendix.

7. Measurements and results

The measurements were taken with a HIL system. HIL systems which are gaining more and more importance, as the possibility of a low-cost and flexible way of validating controls of individual machines up to entire systems have been optimized to date. It is in no way inferior to conventional measurements on significantly less flexible and sometimes expensive measurement setups [46]. In Fig. 8 the picture of the HIL setup is shown. To go more in depth, the evaluation and validation of the theoretical part was done with the HIL402 platform produced by Typhoon electronics. As the used PMSM machine model is a nonlinear one, the course of the current-dependent inductances L_d and L_q can be given to the nonlinear machine model in the HIL schematic environment. This makes it possible to compare the estimated inductance values with the measured real inductance test-bench values very easy, by using the term 'real inductance', the 'emulated inductance' is meant. To evaluate the proposed control method, this inductance has to be known. In the meantime, HIL systems have established themselves as a practicable and indispensable way of testing new controls in industry, without losing any of the informative value of a test bench setup. Fig. 8 shows the schematic HIL setup of the test environment used is shown. The simulation of a traction inverter and a PMSM in the Typhoon HIL402 is made possible within a quasi-real-time environment. The code is written and generated in Matlab/Simulink and compiled into C-code, which is implemented and tested directly. The HIL testbench for recording the measurements and results is the HIL Scada. The measurements are divided into two ranges, the constant torque range and the constant power range. To be able to compare the presented ST-SMC, a conventional PI scheme was presented, which holds the most widespread share of implemented schemes. Comparing the two controls is difficult because the stability and dynamic performance depend on the parameter setting. For the setting of the PI current controller, the setting according to the magnitude optimum was selected. This method is 'best practice' for the PI controller and will not be presented in detail here. Fig. 9 shows the characteristic course for the PMSM under test. It is made clear that the maximum achievable torque for the constant torque range is about 310 N m and decreases, from reaching the corner speed, approximately in an inversely proportional way with respect to the angular velocity. The measurements for the field weakening range were carried out at a speed of 5000 rpm. Here, a maximum achievable torque of 250 N m can be achieved.

Concerning the electrical parameters of the used interior PMSM, see Table 1.

7.1. The constant torque range

The results of the control of the currents in the constant torque range proved to be very similar for both controls. The scheme used in both cases was that shown in Fig. 3 and was applied as a scheme for ST-SMC as well as for PI control. The constant torque

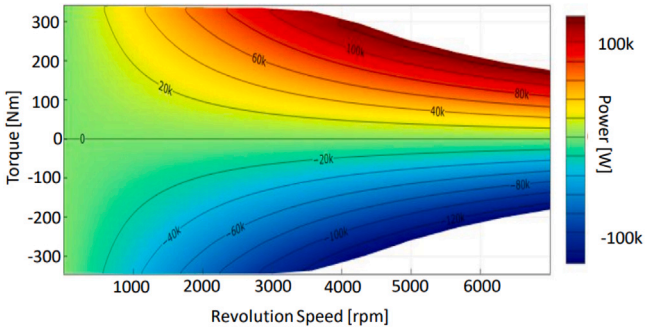

Fig. 9. Characteristic Diagram for PMSM under Test.

Table 1
Parameters of PMSM under test.

PMSM parameters		
flux distribution	sinusoidal	
stator resistance R_s	0.016	Ω
direct inductance L_d	0.223e−3	Hz
quadrature inductance L_q	0.751e−3	Hz
flux induced by magnets Ψ_p	0.058	V s
inertia J	0.071	kg m^{-2}
number of pole pairs p	4	

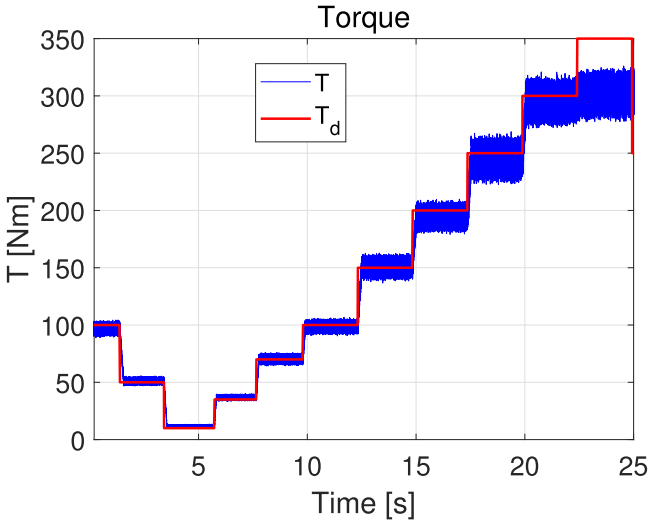

Fig. 10. Torque with ST-SMC for the constant torque range.

range is characterized by the fact that here the control takes place at the current limit. In this range, the setpoints are defined on the basis of the MTPA calculation rule. Fig. 13 shows the result for a conventional PI control, which was set up for a comparison to the ST-SMC. As it can be seen, at the beginning there is a settling process and a slight deviation of the actual value from the setpoint. This can be justified by the fact that the estimated inductance in Figs. 16 and 17 also undergoes a certain transient and the estimate for the target torque is inaccurate towards zero. Fig. 10 on the other hand shows the result for desired and controlled torque with ST-SMC in the constant torque range. Since the results from the estimation of the adaptive KF in Figs. 18 and 19 are much more accurate, the deviation between the nominal and actual torque values is smaller. The estimation seems to work better for the ST-SMC and does not require the use of nominal values in the control for torque requirement to zero. Figs. 14 and 15 show the course of the direct and quadrature currents for PI control in constant power range. While the actual value for the direct current in Fig. 14 follows the nominal value, the actual value for the quadrature current in Fig. 15 experiences a similar deviation as it can be found in the course of the torque in Fig. 13. Figs. 11 and 12 on the other hand show the results for the control with ST-SMC for the constant torque range. It can be seen that there is no deviation between the actual value and the setpoint value for the quadrature current in Fig. 12, which is also reflected in the torque control value in Fig. 10.

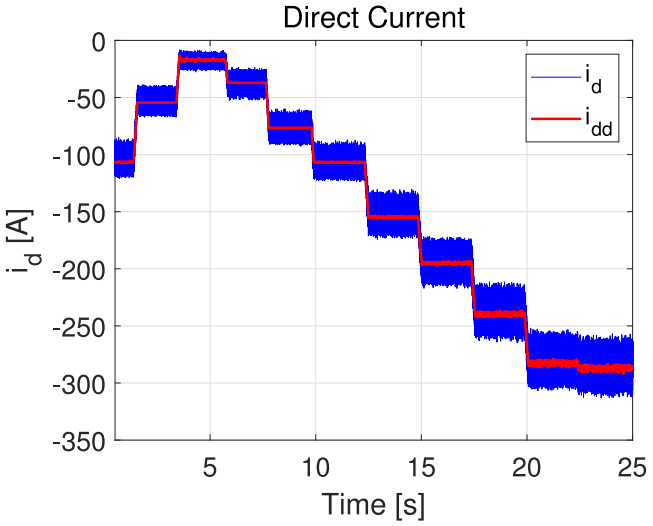

Fig. 11. Direct current with ST-SMC for the constant torque range.

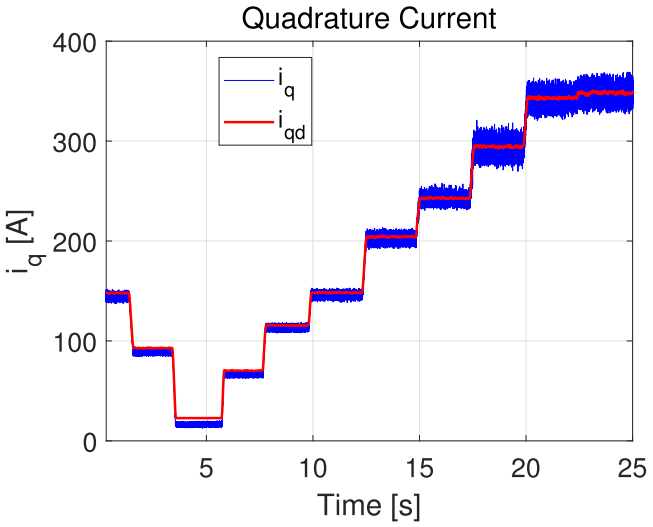

Fig. 12. Quadrature current with ST-SMC for the constant torque range.

7.2. The constant power range

The constant power range measurements were made at a speed of 4500 rpm at which the field weakening control strategy must be active. In order to enable control in the field weakening range, the flux weakening is used instead of the control script of the MTPA, which becomes active in the outer control loop. As can be seen in Fig. 3, the calculation of the voltage not to be exceeded is obtained from the MTPA via the setpoint currents to be determined. In the field weakening range, the control at the voltage limit is active by means of flux weakening, which is achieved by switching from MTPA to range II. For the constant power range, the nominal values of the inductances have to be calculated for the PI controller for feedforward control and could not be used from the estimation of the adaptive KF. In the constant power range, the adaptive EKF tended to be unstable, which increased as the field weakening increased. As to be seen in Figs. 23 and 20, the maximum achievable torque in the field weakening area drops to 250 N m. As already indicated, the EKF could not be applied adaptively for PI control. In order to nevertheless enable a direct comparison of the control with the ST-SMC, the values of the EKF for the inductance were estimated offline and transferred to the PI controller as input for the actual measurement as a table of values. Since the value table is less accurate than for online estimation, the dynamic behavior of the PI controller for decoupling with feedforward is not optimal, as can be seen from the quadrature and direct currents i_d and i_q for control with PI in Figs. 24 and 25. The torque for control with PI in the constant power range shows the

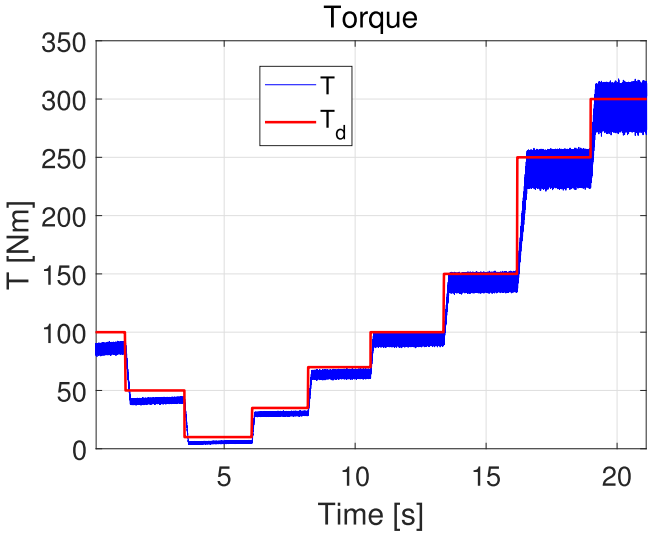

Fig. 13. Torque with PI for the constant torque range.

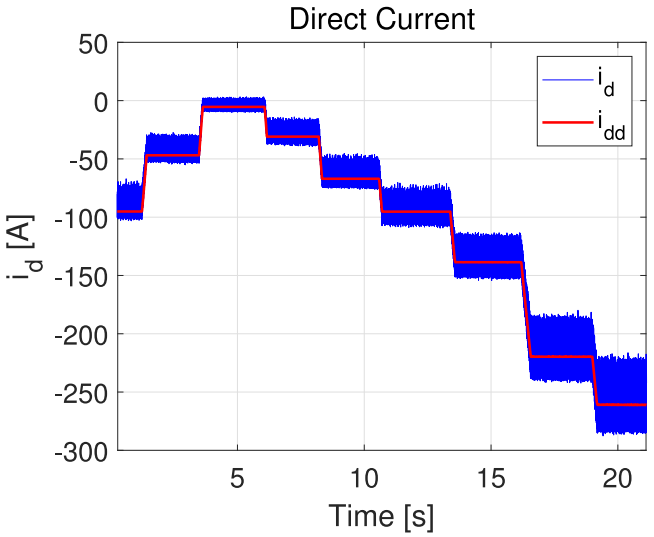

Fig. 14. Direct current with PI for the constant torque range.

same inaccuracy as it is already present for the currents i_d and i_q. The ST-SMC shows good results for the torque in Fig. 20, even though the deviation in the range of zero moment can be seen here, due to the worse estimation by the adaptive EKF. The ST-SMC controlled currents for i_d and i_q follow the setpoints without overshoot and are stationary accurate in a steady state, as can be seen in Figs. 21 and 22.

7.3. Aspects on the choice of the two PI parameters and some detailed results

The most common PI design methods are the symmetrical optimum and the magnitude optimum. The symmetrical optimum method aims to maximize the phase margin, which optimally dampens the closed control loop. In the field of drive technology, this setting rule is often used for the speed control loop, as it results in good disturbance behavior. The magnitude optimum is a design method based on the frequency characteristic curve method that has established itself as a design method for current and torque control loops. The design aims to compensate for the largest time constant of the controlled system and to set the gain of the controller accordingly. This results in a setting with the best possible control behavior. In this context, optimization refers to the optimization of the settling time. Since the PMSM is a cross-coupled system of d-axis and q-axis, when transforming into dq-reference frame, this coupling must first be solved by a decoupling in form of a feedforward control. The feedforward control thus decisively determines the dynamics of the system to be controlled. Only after successful decoupling the PI controller is able to work optimally.

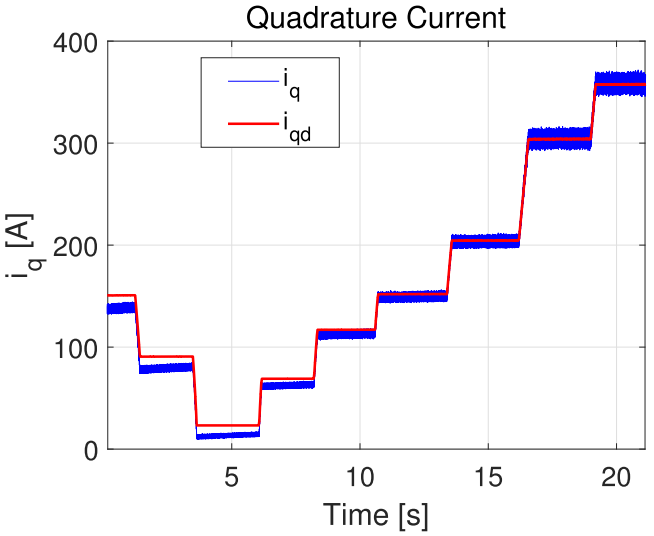

Fig. 15. Quadrature current with PI for the constant torque range.

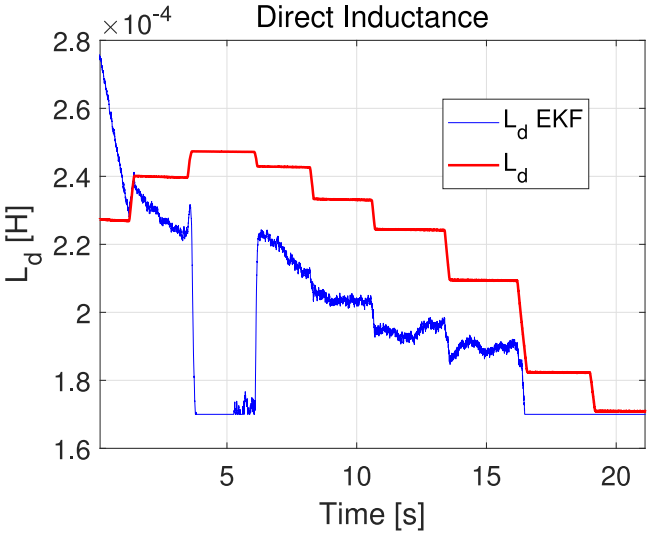

Fig. 16. Estimated direct inductance for the constant torque range in PI control.

In order to achieve the most efficient decoupling of the two axes d and q, it is helpful to know the machine parameters as precisely as possible, what is done by the help of the presented EKF in the described work. The transfer function of the PI controller gain is

$$G(s) = K_{p(d/q)} + K_i \frac{1}{s}. \tag{94}$$

After the coefficient comparison carried out for the magnitude optimum method, the result for the design of the proportional and integral controller gain K_p and K_i is as follows:

$$K_{p(d/q)} = \frac{L_{d/q}}{2\tau_\sigma}, \tag{95}$$

with τ_σ as the dead time resulting from the measurement and calculation time of the closed control loop. For the integral amplification part:

$$K_i = \frac{R_s}{2\tau_\sigma}. \tag{96}$$

A detailed derivation of the method of the magnitude optimum is given in [33]. Using the described strategies, the parameters of Table 2 are obtained to validate the control method. It is to recommend that the calculated gains were scaled to the DC link

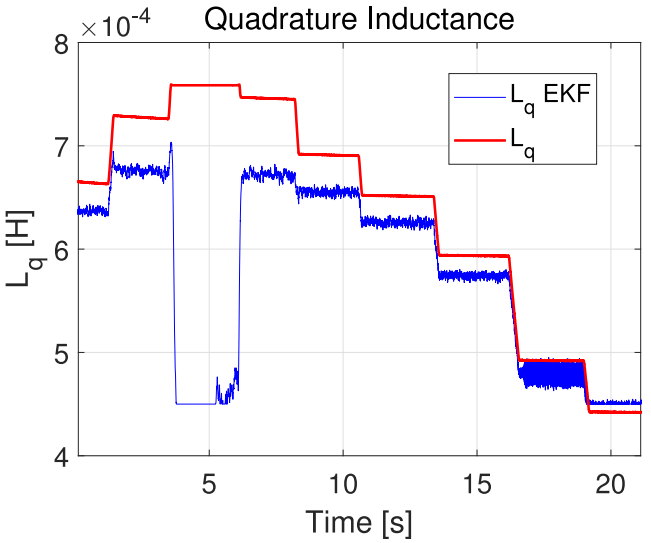

Fig. 17. Estimated quadrature inductance for the constant torque range in PI control.

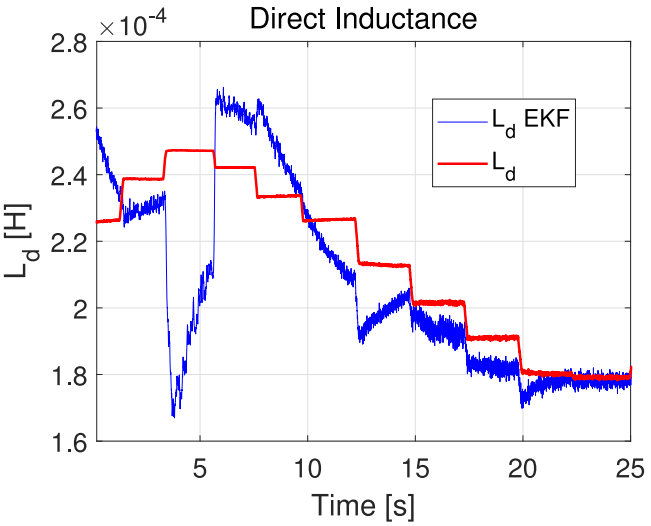

Fig. 18. Estimated direct inductance for the constant torque range with ST-SMC control.

voltage of 600V. To give an index for the control performance, the resulting error for each control structure (ST-SMC and PI), mainly consisting of overshoots and settling time, was given in Table 3. When looking at (97), it can be seen that the resulting error includes the ratio of speed and overshoot of the two control structures as well. The error of resulting currents and torque is calculated with

$$E = \frac{1}{T}\int_0^T e^2(\tau)d\tau. \tag{97}$$

The results are obtained with the following matrices to tune the EKF: measurement noise matrix

$$R_w = \begin{bmatrix} 1e2 & 0 \\ 0 & 1e2 \end{bmatrix}, \tag{98}$$

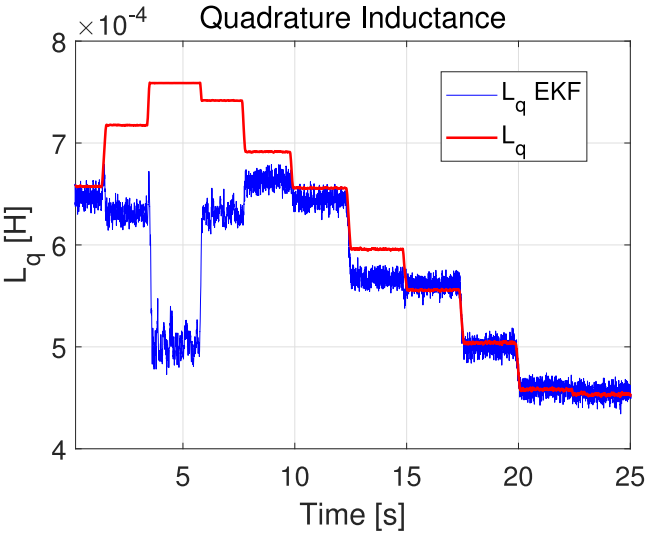

Fig. 19. Estimated quadrature inductance for the constant torque range with ST-SMC control.

Table 2
Control parameters for PMSM control with ST-SMC and PI.

	SMC	PI
Kp_d		0.001
Kp_q		0.005
K_i		0.1
k_d	2	
k_q	2	
U_d	450	
U_q	450	
W_d	$1.1U_d$	
W_q	$1.1U_q$	

process noise matrix

$$Q = \begin{bmatrix} 1e10 & 0 & 0 & 0 \\ 0 & 1e1 & 0 & 0 \\ 0 & 0 & 1e-7 & 0 \\ 0 & 0 & 0 & 1e-4 \end{bmatrix} \tag{99}$$

and the following initial a posteriori error covariance matrix

$$P_0 = \begin{bmatrix} 1 & 0 & 0 & 0 \\ 0 & 1 & 0 & 0 \\ 0 & 0 & 1e-3 & 0 \\ 0 & 0 & 0 & 1e-3 \end{bmatrix}. \tag{100}$$

8. Discussion and analysis

Before concluding, some discussions and analyses concerning the use of HIL to validate results, the role of the EKF, the applied method including hardware, software and validation principles are provided.

8.1. Concerning the use of HIL in the results

To get an overview of various current HIL systems, which are used in industrial applications or in the automotive sector for experimental investigations already in the development phase, [46] provides a very good overview. In the following scenario, the HIL emulator is used to validate the estimation method and adaptive control both in the saturation range and under the influence of cross-coupling effects and spatial harmonics. In order to illustrate the stability of the method, the measurement results are also presented in the constant power range in addition to the constant torque range. Temperature effects and losses in the iron core can be neglected, as the functionality of the control system presented is to be verified. This justifies the use of the HIL emulator

Table 3
Comparison of control performance for PMSM control with ST-SMC and PI.

constant torque range		
	ST-SMC	PI
i_d	22	40
i_q	23	41
T	23	41
constant power range		
	ST-SMC	PI
i_d	18	39
i_q	17	40
T	17	40

$$E = \frac{1}{T}\int_0^T e^2(\tau)d\tau$$

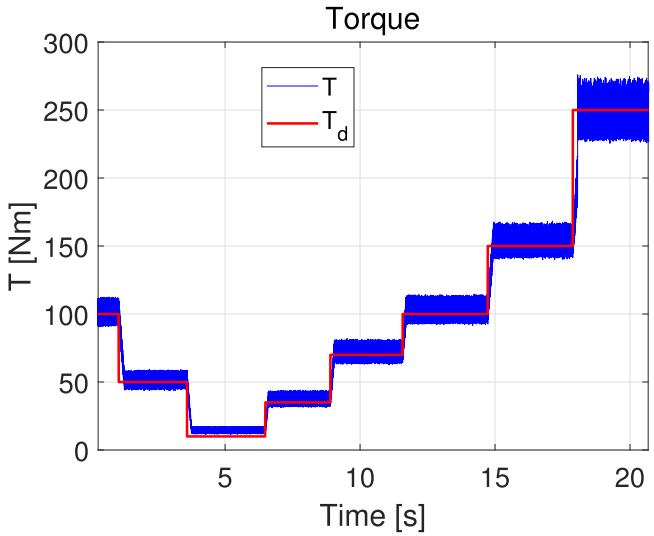

Fig. 20. Torque with ST-SMC for the constant power range.

for experimental testing. The work in [47,48] shows how machine properties can be simulated by mathematical models in the HIL emulator, taking into account cross-coupling effects, magnetic saturation and spatial harmonics. Another point is, that Typhoon HIL uses ideal switches to modulate the inverter. By using ideal switches, there is no tendency to unphysical behavior, which can occur while using model approaches with simplified equivalents. These ideal modulation switches can be parameterized with delay times for the adjustment of the switch-on and switch-off behavior, which was implemented in the underlying work on the basis of the data sheet for the IGBT module SKiM459GD12E4. On the basis of this data sheet, an additional consideration of the losses was made, which was done by taking the typical forward characteristic of the diode and the typical output characteristic of the IGBT. Within the HIL emulator, a linear state space model of each switch is calculated in advance for each switch position during the modulation of the inverter, i.e. all calculations are performed for each switch position.

8.2. Concerning the role of EKF in the results

Showing the role of the EKF, [1] gives an example for a PI control method, where the online identification of the saturated inductances is not considered, especially in the feedforward control, but with the nominal inductances for L_d and L_q. The result is less dynamic behavior due to the lack of decoupling of the d-axis and q-axis of the PMSM. As the nominal values refer to the linear range of the PMSM, [1] shows, that the online identification becomes important in the range of high torque demand. The higher the load, the higher the occurring saturation in the inductance and therefore the deviation from the nominal value is. The decoupling becomes less accurate and overshoots can occur, without using an online parameter identification like an EKF.

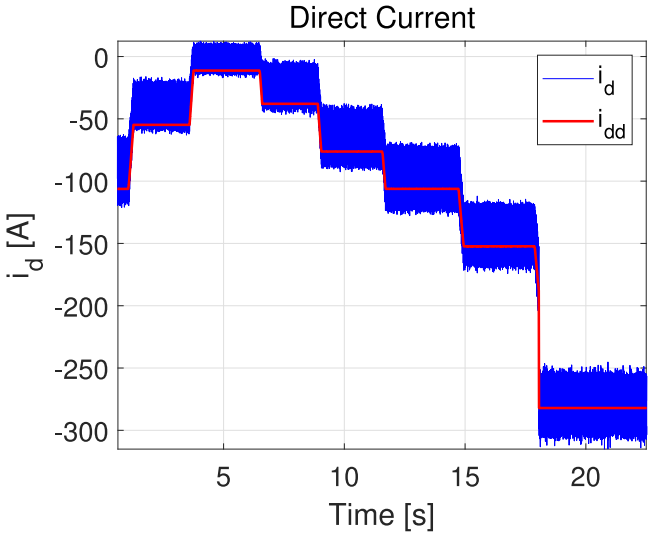

Fig. 21. Direct current with ST-SMC for the constant power range.

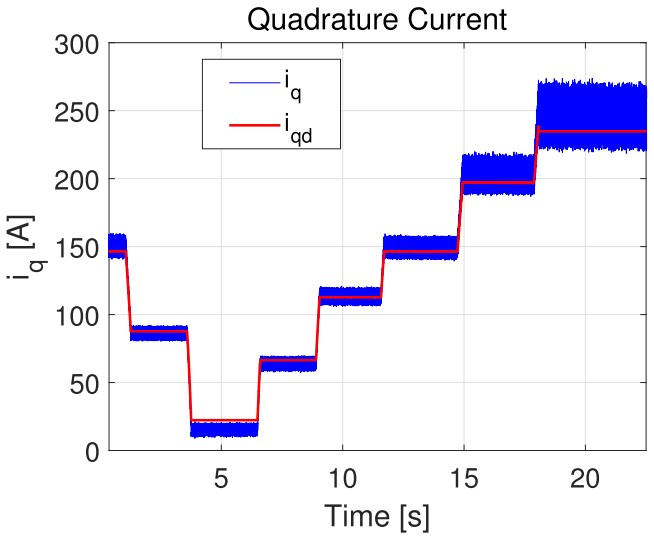

Fig. 22. Quadrature current with ST-SMC for the constant power range.

8.3. Concerning the proposed control strategy in the results

The proposed control structure works with an MTPA and a field weakening control in the outer control loop. Due to the calculation basis of both structures, it follows that this is only valid for PMSMs where L_d is not equal to L_q and thus represents a limitation for PMSMs with surface magnets. The control structure was validated for a PMSM with buried magnets, whereby the underlying inductances are small, so that the PMSM can be regarded as low impedance. It should be noted that the smaller the inductances, the more difficult it is for the EKF to estimate them. For this reason, the underlying control strategy for PMSMs with buried magnets can be considered valid over a wide range.

8.4. Concerning the selection of the ST-SMC and EKF parameters

We have two kinds of specific parameters to identify: the control parameters of the ST-SMC and the tuning parameters of the EKF. Concerning the parameters for the ST-SMC, $U_{(.)}$ and $W_{(.)}$ should be tuned in a way to find a tradeoff between speed of convergence (large enough $U_{(.)}$ and $W_{(.)}$) and feasible input signals (small enough $U_{(.)}$ and $W_{(.)}$) to be realized with standard electrical drives. The HIL system therefore is a great step to detect the best tuning parameters before a test bench measurement, without the risk, that an

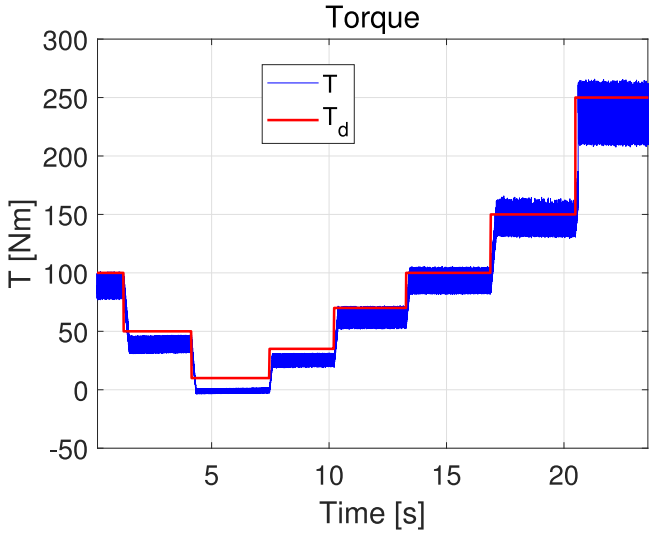

Fig. 23. Torque with PI for the constant power range.

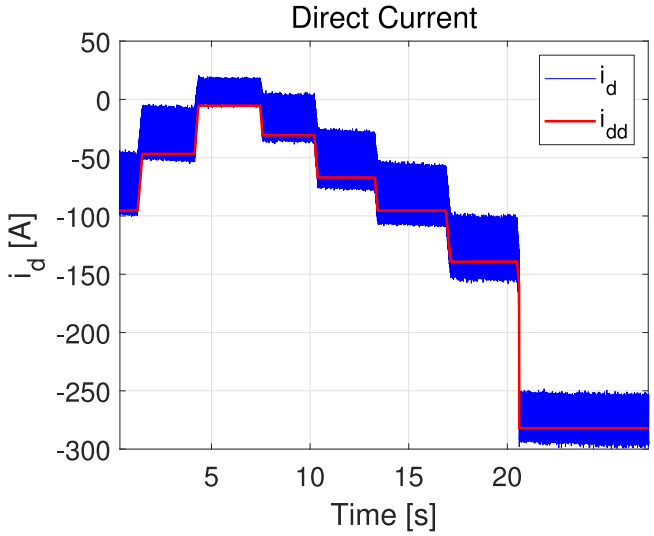

Fig. 24. Direct current with PI for the constant power range.

incorrect setting could lead to a shutdown or even destruction of one of the system-relevant components. The Typhoon HIL then is the scaled electrical drive, where noise and nonlinear saturation effects are emulated with an FPGA.

The most critical parameters are the tuning parameters Q (covariance matrix of the process noise), see (99), R_w (covariance matrix of the measurement noise), see (98) and P_0 (initial a posteriori error covariance matrix), see (100) of the EKF. These parameters are the most important because the correct EKF tuning guarantees stability and controllability by providing the important control parameters for the ST-SMC. These parametric uncertainties can be effectively managed by the EKF through its statistical nature. Figs. 26 and 27 indicate that in the beginning the variances of the errors start decreasing fast and then remain at their possible minima. We cannot guarantee that the EKF obtains the global minima of the errors, as the EKF just approximates the strict hypotheses related to optimality and convergence, see [44]. Nevertheless, using HIL again helps to identify and validate optimal conditions.

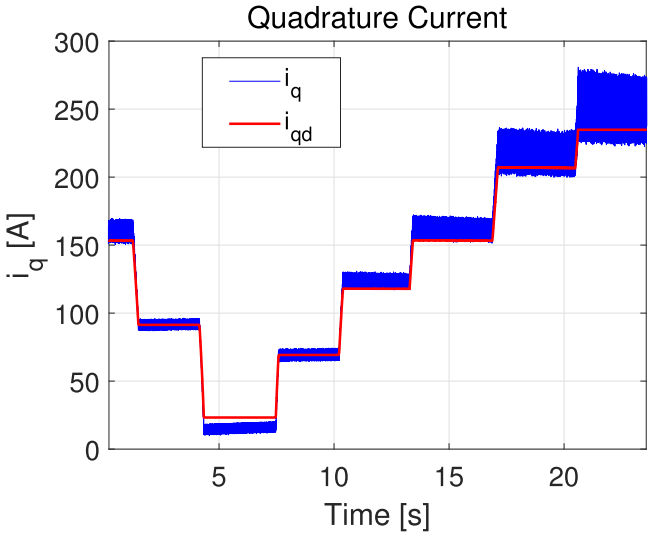

Fig. 25. Quadrature current with PI for the constant power range.

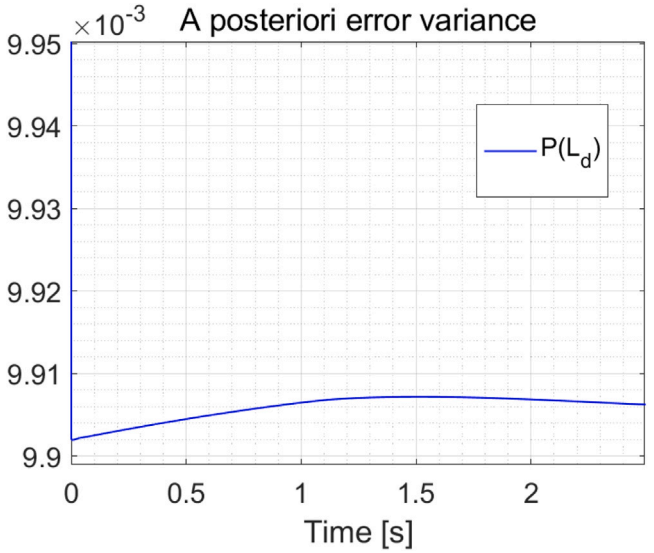

Fig. 26. Course of the error variance matrix of $P(L_d)$.

8.5. Concerning the HIL implementation

The KF and especially the EKF are known for their computationally intensive operations. As Moore's Law predicts, the density of transistors located on an integrated circuit is expected to double every year. This prediction, which has largely come true, has led to the KF being much easier to be used today. Nevertheless, there may be restrictions that make it necessary to limit the sampling time. In [1] an EKF estimation with a backward Euler discretization is presented, which is able to work with a significantly lower number of sampling steps. In [42], on the other hand, the software is implemented on a TI DSP F28335, on which an adaptive EKF estimation with the help of a forward Euler discretization is programmed. When implementing the control strategy, it is therefore important to consider the hardware conditions for the computationally intensive EKF calculations in advance and to take the resulting necessary measures.

9. Conclusion

This paper deals with a sliding mode control together with an extended Kalman filter to robustify optimal control strategies in the context of the torque control. The saturation of the inductance of permanent magnet synchronous machines is considered by

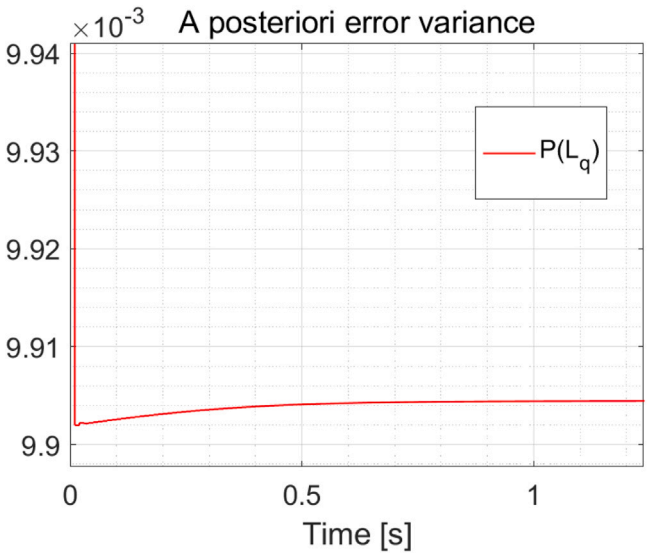

Fig. 27. Course of the error variance matrix of $P(L_q)$.

calculating a bivariate polynomial for L_d and L_q and bringing it into the estimation of the Kalman filter. The control was set up for the constant torque range as well as for the constant power range, where maximum torque per ampere and flux weakening are used in an outer control loop for calculation of the optimum setpoints. The sliding mode control was compared to a proportional integral control which is a conventional control method for permanent magnet synchronous machines. The results were validated by measurements using hardware in the loop with Typhoon HIL402.

CRediT authorship contribution statement

Tanja Zwerger: Writing – review & editing, Writing – original draft, Visualization, Validation, Software, Methodology, Investigation, Formal analysis, Data curation, Conceptualization. **Paolo Mercorelli:** Writing – review & editing, Writing – original draft, Validation, Supervision, Project administration, Methodology, Investigation, Funding acquisition, Formal analysis, Data curation, Conceptualization.

Declaration of competing interest

The authors declare that they have no known competing financial interests or personal relationships that could have appeared to influence the work reported in this paper.

Acknowledgments

We thank the anonymous reviewers for their careful reading of our manuscript and their many insightful comments and suggestions.

Appendix

A.1. Discretization equations

$$J_{f_{13}} = (R_s i_d(k) - \omega_{el}(k) i_q(k) L_q(k) - u_d(k)) \frac{T_s}{L_d^2(k)} \tag{101}$$

$$J_{f_{24}} = (R_s i_q(k) + \omega_{el}(k) i_d(k) L_d(k) + \omega_{el}(k) \Psi_p(k) - u_q(k)) \frac{T_s}{L_q(k)^2} \tag{102}$$

$$J_{f_{31}} = \frac{1}{\left(\frac{R_s T_s}{L_d(k)} + 1\right)\left(\frac{{T_s}^2 \omega_{el}(k)^2}{\left(\frac{R_s T_s}{L_d(k)} + 1\right)\left(\frac{R_s T_s}{L_q(k)} + 1\right)} + 1\right)} \tag{103}$$

$$J_{f_{32}} = T_s \left(\Theta_d(1) \left(\frac{u_d(k)}{L_d(k)} - \frac{R_s\, i_d(k)}{L_d(k)} + \frac{L_q(k)\, i_q(k)\, \omega_{el}(k)}{L_d(k)} \right) - \frac{R_s\, \Theta_d(3)}{L_q(k)} - \frac{R_s\, \Theta_d(1)\, i_d(k)}{L_q(k)} + \frac{L_q(k)\, \Theta_d(2)\, \omega_{el}(k)}{L_d(k)} + \frac{L_q(k)\, \Theta_d(1)\, i_q(k)\, \omega_{el}(k)}{L_d(k)} \right) \tag{104}$$

$$J_{f_{33}} = 1 - T_s \left(\Theta_d(2) \left(\frac{u_d(k)}{L_d(k)^2} - \frac{R_s\, i_d(k)}{L_d(k)^2} + \frac{L_q(k)\, i_q(k)\, \omega_{el}(k)}{L_d(k)^2} \right) + \Theta_d(1)\, i_q(k) \left(\frac{u_d(k)}{L_d(k)^2} - \frac{R_s\, i_d(k)}{L_d(k)^2} + \frac{L_q(k)\, i_q(k)\, \omega_{el}(k)}{L_d(k)^2} \right) + \frac{\Theta_d(1)\, i_d(k)^2\, \omega_{el}(k)}{L_q(k)} + \frac{\Theta_d(3)\, i_d(k)\, \omega_{el}(k)}{L_q(k)} \right) \tag{105}$$

$$J_{f_{34}} = T_s \left(\Theta_d(3) \left(\frac{R_s\, i_q(k)}{L_q(k)^2} - \frac{u_q(k)}{L_q(k)^2} + \frac{\Psi_p\, \omega_{el}(k)}{L_q(k)^2} + \frac{L_d(k)\, i_d(k)\, \omega_{el}(k)}{L_q(k)^2} \right) + \Theta_d(1)\, i_d(k) \left(\frac{R_s\, i_q(k)}{L_q(k)^2} - \frac{u_q(k)}{L_q(k)^2} + \frac{\Psi_p\, \omega_{el}(k)}{L_q(k)^2} + \frac{L_d(k)\, i_d(k)\, \omega_{el}(k)}{L_q(k)^2} \right) + \frac{\Theta_d(1)\, i_q(k)^2\, \omega_{el}(k)}{L_d(k)} + \frac{\Theta_d(2)\, i_q(k)\, \omega_{el}(k)}{L_d(k)} \right) \tag{106}$$

$$J_{f_{41}} = -T_s \left(\Theta_q(1) \left(\frac{R_s\, i_q(k)}{L_q(k)} - \frac{u_q(k)}{L_q(k)} + \frac{\Psi_p\, \omega_{el}(k)}{L_q(k)} + \frac{L_d(k)\, i_d(k)\, \omega_{el}(k)}{L_q(k)} \right) + \frac{R_s\, \Theta_q(2)}{L_d(k)} + \frac{R_s\, \Theta_q(1)\, i_q(k)}{L_d(k)} + \frac{L_d(k)\, \Theta_q(3)\, \omega_{el}(k)}{L_q(k)} + \frac{L_d(k)\, \Theta_q(1)\, i_d(k)\, \omega_{el}(k)}{L_q(k)} \right) \tag{107}$$

$$J_{f_{42}} = T_s \left(\Theta_q(1) \left(\frac{u_d(k)}{L_d(k)} - \frac{R_s\, i_d(k)}{L_d(k)} + \frac{L_q(k)\, i_q(k)\, \omega_{el}(k)}{L_d(k)} \right) - \frac{R_s\, \Theta_q(3)}{L_q(k)} - \frac{R_s\, \Theta_q(1)\, i_d(k)}{L_q(k)} + \frac{L_q(k)\, \Theta_q(2)\, \omega_{el}(k)}{L_d(k)} + \frac{L_q(k)\, \Theta_q(1)\, i_q(k)\, \omega_{el}(k)}{L_d(k)} \right) \tag{108}$$

$$J_{f_{43}} = -T_s \left(\Theta_q(2) \left(\frac{u_d(k)}{L_d(k)^2} - \frac{R_s\, i_d(k)}{L_d(k)^2} + \frac{L_q(k)\, i_q(k)\, \omega_{el}(k)}{L_d(k)^2} \right) + \Theta_q(1)\, i_q(k) \left(\frac{u_d(k)}{L_d(k)^2} - \frac{R_s\, i_d(k)}{L_d(k)^2} + \frac{L_q(k)\, i_q(k)\, \omega_{el}(k)}{L_d(k)^2} \right) + \frac{\Theta_q(1)\, i_d(k)^2\, \omega_{el}(k)}{L_q(k)} + \frac{\Theta_q(3)\, i_d(k)\, \omega_{el}(k)}{L_q(k)} \right) \tag{109}$$

$$J_{f_{44}} = T_s \left(\Theta_q(3) \left(\frac{R_s\, i_q(k)}{L_q(k)^2} - \frac{u_q(k)}{L_q(k)^2} + \frac{\Psi_p\, \omega_{el}(k)}{L_q(k)^2} + \frac{L_d(k)\, i_d(k)\, \omega_{el}(k)}{L_q(k)^2} \right) + \Theta_q(1)\, i_d(k) \left(\frac{R_s\, i_q(k)}{L_q(k)^2} - \frac{u_q(k)}{L_q(k)^2} + \frac{\Psi_p\, \omega_{el}(k)}{L_q(k)^2} + \frac{L_d(k)\, i_d(k)\, \omega_{el}(k)}{L_q(k)^2} \right) + \frac{\Theta_q(1)\, i_q(k)^2\, \omega_{el}(k)}{L_d(k)} + \frac{\Theta_q(2)\, i_q(k)\, \omega_{el}(k)}{L_d(k)} \right) + 1. \tag{110}$$

References

[1] T. Zwerger, P. Mercorelli, Backward extended Kalman filter to estimate and adaptively control a PMSM in saturation conditions, IEEE J. Emerg. Sel. Top. Ind. Electron. (2023) 1–14, http://dx.doi.org/10.1109/JESTIE.2023.3313066.

[2] J. Song, W.X. Zheng, Y. Niu, Self-triggered sliding mode control for networked PMSM speed regulation system: A PSO-optimized super-twisting algorithm, IEEE Trans. Ind. Electron. 69 (1) (2022) 763–773, http://dx.doi.org/10.1109/TIE.2021.3050348.

[3] J. Song, Y.-K. Wang, Y. Niu, H.-K. Lam, S. He, H. Liu, Periodic event-triggered terminal sliding mode speed control for networked PMSM system: A GA-optimized extended state observer approach, IEEE/ASME Trans. Mechatron. 27 (5) (2022) 4153–4164, http://dx.doi.org/10.1109/TMECH.2022.3148541.

[4] T.M. Jahns, G.B. Kliman, T.W. Neumann, Interior permanent-magnet synchronous motors for adjustable-speed drives, IEEE Trans. Ind. Appl. IA-22 (4) (1986) 738–747, http://dx.doi.org/10.1109/TIA.1986.4504786.

[5] S. Bolognani, L. Tubiana, M. Zigliotto, EKF-based sensorless IPM synchronous motor drive for flux-weakening applications, IEEE Trans. Ind. Appl. 39 (3) (2003) 768–775, http://dx.doi.org/10.1109/TIA.2003.810666.

[6] A. Levant, Sliding order and sliding accuracy in sliding mode control, Internat. J. Control 58 (6) (1993) 1247–1263, http://dx.doi.org/10.1080/00207179308923053.

[7] Y.-C. Liu, S. Laghrouche, A. N'Diaye, M. Cirrincione, Hermite neural network-based second-order sliding-mode control of synchronous reluctance motor drive systems, J. Franklin Inst. 358 (1) (2021) 400–427, http://dx.doi.org/10.1016/j.jfranklin.2020.10.029, URL https://www.sciencedirect.com/science/article/pii/S0016003220307341.

[8] S. Bouyahia, S. Semcheddine, B. Talbi, O. Boutalbi, Y. Terchi, An adaptive super-twisting sliding mode algorithm for robust control of a biotechnological process, Int. J. Dyn. 8 (2) (2019) 581–591, http://dx.doi.org/10.1007/s40435-019-00551-8, URL http://dx.doi.org/10.1007/s40435-019-00551-8.

[9] Z. Feng, J. Fei, Design and analysis of adaptive super-twisting sliding mode control for a microgyroscope, PLoS One 13 (1) (2018) e0189457, http://dx.doi.org/10.1371/journal.pone.0189457, URL http://dx.doi.org/10.1371/journal.pone.0189457.

[10] C. Xu, K. Wang, Y. Wang, C. Chen, B. Zhang, Super-twisting sliding mode control of permanent magnet synchronous motor based on predictive adaptive law, in: 2021 IEEE 5th Advanced Information Technology, Electronic and Automation Control Conference, IAEAC, IEEE, 2021, http://dx.doi.org/10.1109/iaeac50856.2021.9391016.

[11] J. Gu, S. You, W. Kim, J. Moon, Fuzzy event-triggered super twisting sliding mode control for position tracking of permanent magnet synchronous motors under unknown disturbances, IEEE Trans. Ind. Inform. 19 (9) (2023) 9843–9854, http://dx.doi.org/10.1109/tii.2022.3231410.

[12] H. Yang, Y. Bai, Y.-R. Chien, Generalized super-twisting sliding mode control of permanent magnet synchronous motor based on sinusoidal saturation function, IEICE Electron. Express 19 (9) (2022) 20220066, http://dx.doi.org/10.1587/elex.19.20220066.

[13] H. Dong, X. Yang, Z. Kuang, M. Liu, On practical terminal sliding-mode control for systems with or without mismatched uncertainty, J. Franklin Inst. 359 (15) (2022) 8084–8106, http://dx.doi.org/10.1016/j.jfranklin.2022.07.007, URL https://www.sciencedirect.com/science/article/pii/S0016003222004665.

[14] Z. Li, J. Wang, S. Wang, S. Feng, Y. Zhu, H. Sun, Design of sensorless speed control system for permanent magnet linear synchronous motor based on fuzzy super-twisted sliding mode observer, Electronics 11 (9) (2022) 1394, http://dx.doi.org/10.3390/electronics11091394.

[15] H. Qiu, H. Zhang, L. Min, T. Ma, Z. Zhang, Adaptive control method of sensorless permanent magnet synchronous motor based on super-twisting sliding mode algorithm, Electronics 11 (19) (2022) 3046, http://dx.doi.org/10.3390/electronics11193046.

[16] J. Hu, H. Lu, B. Zheng, Y. Zhang, Predictive control of permanent magnet synchronous motor based on Super-Twisting sliding mode, Energy Sci. Eng. 11 (9) (2023) 3173–3184, http://dx.doi.org/10.1002/ese3.1512.

[17] S. Luo, R. Gao, Chaos control of the permanent magnet synchronous motor with time-varying delay by using adaptive sliding mode control based on DSC, J. Franklin Inst. 355 (10) (2018) 4147–4163, http://dx.doi.org/10.1016/j.jfranklin.2018.04.031, URL https://www.sciencedirect.com/science/article/pii/S0016003218302692.

[18] Y.-C. Liu, S. Laghrouche, D. Depernet, A. N'Diaye, A. Djerdir, M. Cirrincione, Super-twisting sliding-mode observer-based model reference adaptive speed control for PMSM drives, J. Franklin Inst. 360 (2) (2023) 985–1004, http://dx.doi.org/10.1016/j.jfranklin.2022.12.014, URL https://www.sciencedirect.com/science/article/pii/S0016003222008833.

[19] X. Li, J. Liu, Y. Yin, K. Zhao, Improved super-twisting non-singular fast terminal sliding mode control of interior permanent magnet synchronous motor considering time-varying disturbance of the system, IEEE Access 11 (2023) 17485–17496, http://dx.doi.org/10.1109/access.2023.3244190.

[20] X. mei Zhao, Y. wei Gong, H. yan Jin, C. Xu, Adaptive super-twisting-based nonsingular fast terminal sliding mode control of permanent magnet linear synchronous motor, Trans. Inst. Meas. Control (2023) 014233122311627, http://dx.doi.org/10.1177/01423312231162782.

[21] S. Du, S. Wang, Y. Wang, L. Jia, W. Sun, Y. Liu, Design of sensorless control system for permanent magnet linear synchronous motor based on parametric optimization super-twisting sliding mode observer, Electronics 12 (12) (2023) 2553, http://dx.doi.org/10.3390/electronics12122553.

[22] M. Hu, H. Ahn, Y. Chung, K. You, Speed regulation for PMSM with super-twisting sliding-mode controller via disturbance observer, Mathematics 11 (7) (2023) 1618, http://dx.doi.org/10.3390/math11071618.

[23] Z.Q. Zhu, D. Liang, K. Liu, Online parameter estimation for permanent magnet synchronous machines: An overview, IEEE Access 9 (2021) 59059–59084, http://dx.doi.org/10.1109/ACCESS.2021.3072959.

[24] P. Mercorelli, A motion-sensorless control for intake valves in combustion engines, IEEE Trans. Ind. Electron. 64 (4) (2017) 3402–3412, http://dx.doi.org/10.1109/TIE.2016.2598314.

[25] P. Mercorelli, A hysteresis hybrid extended Kalman filter as an observer for sensorless valve control in camless internal combustion engines, IEEE Trans. Ind. Appl. 48 (6) (2012) 1940–1949.

[26] P. Mercorelli, A two-stage augmented extended Kalman filter as an observer for sensorless valve control in camless internal combustion engines, IEEE Trans. Ind. Electron. 59 (11) (2012) 4236–4247.

[27] P. Mercorelli, A two-stage sliding-mode high-gain observer to reduce uncertainties and disturbances effects for sensorless control in automotive applications, IEEE Trans. Ind. Electron. 62 (9) (2015) 5929–5940.

[28] M. Taherzadeh, M.A. Hamida, M. Ghanes, M. Koteich, A new torque observation technique for a PMSM considering unknown magnetic conditions, IEEE Trans. Ind. Electron. 68 (3) (2021) 1961–1971, http://dx.doi.org/10.1109/TIE.2020.2972429.

[29] L. Sepulchre, M. Fadel, M. Pietrzak-David, G. Porte, MTPV flux-weakening strategy for PMSM high speed drive, IEEE Trans. Ind. Appl. 54 (6) (2018) 6081–6089, http://dx.doi.org/10.1109/TIA.2018.2856841.

[30] Z. Xia, S. Nalakath, R. Tarvirdilu-Asl, Y. Sun, J. Wiseman, A. Emadi, Online optimal tracking method for interior permanent magnet machines with improved MTPA and MTPV in whole speed and torque ranges, IEEE Trans. Power Electron. 35 (9) (2020) 9753–9769, http://dx.doi.org/10.1109/TPEL.2020.2970111.

[31] H. Mahmoud, G. Bacco, M. Degano, N. Bianchi, C. Gerada, Synchronous reluctance motor iron losses: Considering machine nonlinearity at MTPA, FW, and MTPV operating conditions, IEEE Trans. Energy Convers. 33 (3) (2018) 1402–1410, http://dx.doi.org/10.1109/TEC.2018.2811543.

[32] Q. Xu, L. Cai, Developing an approach in calculating reference currents for field-weakening control, IEEE Trans. Transp. Electr. 9 (1) (2023) 60–74, http://dx.doi.org/10.1109/TTE.2022.3174707.

[33] Schroeder, Elektrische Antriebe-Regelung von Antriebssystemen, vol. 4, Springer Verlag, Heidelberg, 2015, pp. 1095–1105.

[34] Z. Liu, Y. Han, G. Feng, N.C. Kar, Efficient nonlinear multi-parameter decoupled estimation of PMSM drives based on multi-state voltage and torque measurements, IEEE Trans. Energy Convers. 38 (1) (2023) 321–331, http://dx.doi.org/10.1109/TEC.2022.3187130.

[35] C.D. Denny, P.R. Kumar, E. Jasmin, Super twisting algorithm based slip ratio control of electric vehicles, in: 2020 IEEE International Power and Renewable Energy Conference, 2020, pp. 1–6, http://dx.doi.org/10.1109/IPRECON49514.2020.9315231.

[36] A.F. Filippov, Application of Theory of Differential Equations with Discontinuous Right-Hand Side to Nonlinear Control Problems, World Scientific, Moscow, 1960.

[37] J.-J.E. Slotine, W. Li, Applied Nonlinear Control, Pearson Education Taiwan, 1991.

[38] C. Xu, K. Wang, Y. Wang, C. Chen, B. Zhang, Super-twisting sliding mode control of permanent magnet synchronous motor based on predictive adaptive law, in: 2021 IEEE 5th Advanced Information Technology, Electronic and Automation Control Conference, IAEAC, 2021, pp. 2731–2736, http://dx.doi.org/10.1109/IAEAC50856.2021.9391016.

[39] O. Kruse, A. Mukhamejanova, P. Mercorelli, Super-twisting sliding mode control for differential steering systems in vehicular yaw tracking motion, Electronics 11 (9) (2022) 1330, http://dx.doi.org/10.3390/electronics11091330.
[40] O. Kruse, A. Mukhamejanova, P. Mercorelli, Differential steering system for vehicular yaw tracking motion with help of sliding mode control, in: 2022 23rd International Carpathian Control Conference, ICCC, 2022, pp. 58–63, http://dx.doi.org/10.1109/ICCC54292.2022.9805966.
[41] J.A. Moreno, M. Osorio, Strict Lyapunov functions for the super-twisting algorithm, IEEE Trans. Automat. Contr. 57 (4) (2012) 1035–1040, http://dx.doi.org/10.1109/TAC.2012.2186179.
[42] T. Zwerger, P. Mercorelli, Using a bivariate polynomial in an EKF for state and inductance estimations in the presence of saturation effects to adaptively control a PMSM, IEEE Access 10 (2022) 111545–111553, http://dx.doi.org/10.1109/ACCESS.2022.3215511.
[43] H. Liu, F. Hu, J. Su, X. Wei, R. Qin, Comparisons on Kalman-filter-based dynamic state estimation algorithms of power systems, IEEE Access 8 (2020) 51035–51043, http://dx.doi.org/10.1109/ACCESS.2020.2979735.
[44] G. Welch, G. Bishop, An Introduction to the Kalman Filter, Prentice Hall, Chapel Hill, NC, USA, Univ. North Caroline Chapel Hill, 1995.
[45] T. Zwerger, P. Mercorelli, Combining SMC and MTPA using an EKF to estimate parameters and states of an interior PMSM, in: 2019 20th International Carpathian Control Conference, ICCC, 2019, pp. 1–6, http://dx.doi.org/10.1109/CarpathianCC.2019.8766063.
[46] J.S. Lee, G. Choi, Modeling and hardware-in-the-loop system realization of electric machine drives: A review, CES Trans. Electr. Mach. Syst. 5 (3) (2021) 194–201, http://dx.doi.org/10.30941/CESTEMS.2021.00023.
[47] X. Chen, J. Wang, B. Sen, P. Lazari, T. Sun, A high-fidelity and computationally efficient model for interior permanent-magnet machines considering the magnetic saturation, spatial harmonics, and iron loss effect, IEEE Trans. Ind. Electron. 62 (7) (2015) 4044–4055, http://dx.doi.org/10.1109/TIE.2014.2388200.
[48] N. Bianchi, L. Alberti, MMF harmonics effect on the embedded FE analytical computation of PM motors, IEEE Trans. Ind. Appl. 46 (2) (2010) 812–820, http://dx.doi.org/10.1109/TIA.2010.2041098.